

Clustering of luminous red galaxies I: large scale redshift space distortions

Anna Cabré* and Enrique Gaztañaga†
*Institut de Ciències de l'Espai, CSIC/IEEC, Campus UAB,
 F. de Ciències, Torre C5 par-2, Barcelona 08193, Spain*

This is the first paper of a series where we study the clustering of LRG galaxies in the latest spectroscopic SDSS data release, DR6, which has 75000 LRG galaxies covering over $1 \text{ Gpc}^3/h^3$ at $0.15 < z < 0.47$. Here we focus on modelling redshift space distortions in $\xi(\pi, \sigma)$, the 2-point correlation in separate line-of-sight and perpendicular directions, at large scales and away from the line-of-sight. We use large mock simulations to study the validity of models and errors. We show that errors in the data are dominated by a shot-noise term that is 40% larger than the Poisson error commonly used. We first use the normalized quadrupole to estimate $\beta = f(\Omega_m)/b = 0.34 \pm 0.03$, where $f(\Omega_m)$ is the linear velocity growth factor and b is the linear bias parameter that relates galaxy to matter fluctuations on large scales. We next use the full $\xi(\pi, \sigma)$ plane to find $\Omega_m = 0.245 \pm 0.020$ and the biased amplitude $b\sigma_8 = 1.56 \pm 0.09$. For standard gravity, we can combine these measurements to break degeneracies and find $\sigma_8 = 0.85 \pm 0.06$, $b = 1.85 \pm 0.25$ and $f(\Omega_m) = 0.64 \pm 0.09$ for the whole sample (mean $z = 0.34$). We present constraints for modified theories of gravity and find that standard gravity is consistent with data as long as $0.80 < \sigma_8 < 0.92$. We also calculate the cross-correlation with WMAP5 and show how both methods to measure the growth history are complementary to constrain non-standard models of gravity. Finally, we show results for different redshift slices, including a prominent BAO peak in the monopole at different redshifts. The $\xi(\pi, \sigma)$ data on large scales is shown to be in remarkable agreement with predictions and shows a characteristic large region of negative correlation in the line of sight, a BAO ring and a prominent radial BAO peak. The significance of this is presented in paper IV of this series. We include a study of possible systematic effects in our analysis to find that these results are quite robust.

I. INTRODUCTION

Galaxy clustering allows the study of different physical phenomena at each scale. On large scales density fluctuations are small and can be modeled by linear theory to constrain cosmological parameters. We need large surveys with galaxy positions to do this.

The measured redshift distance s of a galaxy differs from the true radial distance r by its peculiar velocity along the line-of-sight v_r . These displacements lead to redshift distortions, with two important contributions. The first, on large scale fluctuations, caused by coherent bulk motion. We see walls denser and voids bigger and emptier, with a squashing effect in the 2-point correlation function along the line-of-sight: known as the Kaiser [1] effect. At small scales, random velocities inside clusters and groups of galaxies produce a radial stretching pointed at the observer, known as fingers of God (FOG).

Although such distortions complicate the interpretation of redshift maps as positional maps, they have the advantage of bearing unique information about the dynamics of galaxies. In particular, the amplitude of distortions on large scales yields a measure of the linear redshift distortion parameter β , which is related to the matter density, and gives direct information on the growth

of the newtonian gravitational potential $f(\Omega)$ and bias b (see Eq.3).

In this work we use the most recent luminous red galaxies (LRGs) from the spectroscopic SDSS public data release DR6 (Adelman-McCarthy et al. [2]), and perform studies of linear bias at large scales to obtain cosmological parameters. As we will see, we can break the degeneracy between *bias* and σ_8 present in the correlation function thanks to redshift distortions anisotropies, and look at the growth history and possible modifications of the gravity (see Linder [3], Guzzo et al. [4] and the recent Yamamoto et al. [5]). We have cross-correlated LRGs with WMAP in order to investigate the ISW effect, reproducing a high signal as recent studies (see Giannantonio et al. [6] for a compilation of last results), compared to current Λ CDM model. We can also break the *bias* – σ_8 degeneracy and study the growth history using the cross-correlation between temperature of CMB and galaxies w_{TG} , both from another point of view than the used in redshift distortions.

The same LRGs (but with reduced area) have been studied from different points of view. Tegmark et al. [7] have done an analysis of the power spectrum at large scales to obtain cosmological parameters. Zehavi et al. [8] study LRGs at intermediate scales (0.3 to 40Mpc/h), where they calculate the projected correlation function, the monopole and real-space correlation function to study mainly the linear high bias, the non-linear bias and the differences between luminosities, remarking that there are differences from a power law for scales smaller than 1Mpc/h.

*Electronic address: cabre@ieec.uab.es

†Electronic address: gazta@ice.cat

While we were working on our results, a very interesting paper by Okumura et al. [9] showed the first application of the anisotropy in the 2-point correlation function including the baryonic features, to obtain constraints in cosmological parameters. They use the DR3 spectroscopic sample of LRGs to calculate the 2-point correlation function with a different definition than the one used here (Matsubara [10]) and fit $\xi(\sigma, \pi)$ for large scales using the linear Kaiser model, from 40Mpc/h to 200Mpc/h, excluding the FOG zone. They point out that a direct measurement of the growth function can be obtained from Kaiser anisotropy, while $D_a(z)$ and $H(z)$ can be found from the anisotropic baryon acoustic peak, with improved LRG data. Although constraints are weak by now, the fitting of all the anisotropic 2-point correlation function, including the baryonic feature, would enable to divide the effect of redshift distortions into dynamical and geometrical components. The anisotropy due to geometric distortion contributes to better estimation of the equation of state of the dark energy.

There has already been significant progress in this direction using LRG. Eisenstein et al. [11] detected the baryon acoustic peak in the 2-point correlation function using LRGs. Hütsi [12, 13] use LRGs to constrain cosmological parameters in the power spectrum, including the baryonic peak. Percival et al. [14] have analyzed also the LRGs using both 2dF and SDSS. Padmanabhan et al. [15] used the photometric catalog to work with a bigger set of LRGs with photometric redshifts, obtaining also cosmological constraints, the same as Blake et al. [16], which work with the MegaZ-LRG, a photometric-redshift catalog of luminous red galaxies based on the imaging data of the SDSS DR4.

This is the first and main paper of a series on clustering of LRG. Here we will focus on redshift space distortions in $\xi(\pi, \sigma)$ on large scales. In Paper II [17] we will look at small scales in $\xi(\pi, \sigma)$ and address the issue of the FOG. In Paper III [18] we look at the 3-point function and in Paper IV we will focus on the significance of the BAO detections. In this first paper we present the basis for the error analysis and the study of systematics effects that will be used in the rest of the series.

The paper is organized as follows. After this introduction, section II gives a summary of the formulas that we will use in this paper. Section III is devoted to present the mock simulations, error analysis and validation methods. In section IV we present the LRG samples used in our analysis in section V. As usual, we end with discussion and conclusion. In the Appendix we present a study of possible systematic effects.

II. THEORY

Kaiser [1] pointed out that, in the large-scale linear regime, and in the plane-parallel approximation (where galaxies are taken to be sufficiently far away from the observer that the displacements induced by peculiar ve-

locities are effectively parallel), the distortion caused by coherent infall velocities takes a particularly simple form in Fourier space:

$$P_s(k) = (1 + \beta\mu_k^2)^2 P(k). \quad (1)$$

where $P(k)$ is the power spectrum of density fluctuations δ , μ is the cosine of the angle between k and the line-of-sight, the subscript s indicates redshift space, and β is proportional to the velocity growth rate in linear theory.

If the galaxy overdensity δ is linearly biased by a factor b relative to the underlying matter density δ_m of the Universe,

$$\delta = b\delta_m, \quad (2)$$

then the observed value of β is

$$\beta = \frac{f(\Omega_m)}{b} \equiv \frac{1}{b} \frac{d \ln D}{d \ln a} \quad (3)$$

where D is the linear density growth factor and f the velocity growth rate, which we can write as:

$$f(\Omega_m) = \Omega_m(a)^\gamma \quad (4)$$

where γ is the gravitational growth index Linder [3], $\Omega_m(a)$ is the matter density at a redshift z where $a = 1/(1+z)$,

$$\Omega_m(a) = \frac{H_0^2 \Omega_{0m} a^{-3}}{H^2(a)} \quad (5)$$

and

$$H(a) = H_0 \sqrt{\Omega_{0m} a^{-3} + (1 - \Omega_{0m}) a^{-3(1+w)}} \quad (6)$$

By construction [3], the growth index formalism separates out two physical effects on the growth of structure: $\Omega(a)$ involves the expansion history and γ focuses on the gravity theory. The value $\gamma = 0.55$ corresponds to standard gravity, while γ is different for modified gravity, for example $\gamma = 0.68$ in the braneworld cosmology. The linear density growth factor can be found using Eq.3:

$$D(a) = e^{\int_0^a d \ln a [\Omega(a)^\gamma - 1]} \quad (7)$$

A. Modelling $\xi(\sigma, \pi)$

Hamilton [19] translated Kaiser results into real space,

$$\xi'(\sigma, \pi) = \xi_0(s)P_0(\mu) + \xi_2(s)P_2(\mu) + \xi_4(s)P_4(\mu), \quad (8)$$

where π is the separation along the line-of-sight (LOS) and σ across the sky, the absolute distance of separation is $s = \sqrt{\sigma^2 + \pi^2}$, μ is the cosine of the angle between s and the line-of-sight and P_ℓ are Legendre polynomials.

In general (see also Eq.(16)),

$$\xi_0(s) = \left(1 + \frac{2\beta}{3} + \frac{\beta^2}{5}\right) \xi(r), \quad (9)$$

$$\xi_2(s) = \left(\frac{4\beta}{3} + \frac{4\beta^2}{7}\right) [\xi(r) - \bar{\xi}(r)], \quad (10)$$

$$\xi_4(s) = \frac{8\beta^2}{35} \left[\xi(r) + \frac{5}{2}\bar{\xi}(r) - \frac{7}{2}\bar{\bar{\xi}}(r)\right], \quad (11)$$

and

$$\bar{\xi}(r) = \frac{3}{r^3} \int_0^r \xi(r') r'^2 dr', \quad (12)$$

$$\bar{\bar{\xi}}(r) = \frac{5}{r^5} \int_0^r \xi(r') r'^4 dr'. \quad (13)$$

We use these relations to create a model $\xi'(\sigma, \pi)$. Then we convolve it with the distribution function of random pairwise velocities, $f(v)$, to give the final model $\xi(\sigma, \pi)$ (Peebles [20]):

$$\xi(\sigma, \pi) = \int_{-\infty}^{\infty} \xi'(\sigma, \pi - v/H(z)/a(z)) f(v) dv \quad (14)$$

where we divide peculiar velocities by $a(z)$ to translate to comoving distances, since velocities are defined in physical coordinates.

We represent the random motions by an exponential form,

$$f(v) = \frac{1}{\sigma_v \sqrt{2}} \exp\left(-\frac{\sqrt{2}|v|}{\sigma_v}\right) \quad (15)$$

where σ_v is the pairwise peculiar velocity dispersion. An exponential form for the random motions has been found to fit the observed data better than other functional forms (Ratcliffe et al. [21], Landy [22]). We have also checked this relation with our simulations, which will be described later on.

Matsubara [10] and Scoccimarro [23] have presented different models for the 2-point correlation function in redshift space. Tinker et al. [24] and Tinker [25] do a modelling of redshift space distortions in the context of halo occupation distribution model (HOD). These models are complementary to the one studied here. In most situations the differences are small and we will show that our modelling gives good agreement with simulations and real data.

B. Multipoles of $\xi(\sigma, \pi)$

We can define the multipoles of $\xi(\pi, \sigma)$ as

$$\xi_\ell(s) = \frac{2\ell+1}{2} \int_{-1}^{+1} \xi(\pi, \sigma) P_\ell(\mu) d\mu. \quad (16)$$

where μ is cosine of the angle to the line-of-sight π . The normalized quadrupole (Hamilton [19]) is defined as

$$Q(s) = \frac{\xi_2(s)}{\xi_0(s) - (3/s^2) \int_0^s \xi_0(s') s'^2 ds'} \quad (17)$$

Linear bias in Eq.2 cancels in the quadrupole, and $Q(s)$ is only very slightly dependent on the shape of the correlation function, such as changes of Ω_m in large scales or scale dependent non-linear bias for small scales.

In the Kaiser approximation, ie at large scales, the quadrupole is directly related to β

$$Q(s) = \frac{\frac{4}{3}\beta + \frac{4}{7}\beta^2}{1 + \frac{2}{3}\beta + \frac{1}{5}\beta^2} \quad (18)$$

At small scales, the quadrupole depends strongly on the random pairwise velocities, represented by σ_v , but it does not depend much on non-linear bias, as we will show.

C. The real-space correlation function $\xi(r)$

We can estimate the real-space correlation function by calculating the projected correlation function, $\Xi(\sigma)$, integrating the redshift distorted $\xi(\sigma, \pi)$ along the line-of-sight π .

$$\Xi(\sigma) = 2 \int_{\pi=0}^{\pi_{max}=\infty} \xi(\sigma, \pi) d\pi \quad (19)$$

We would like $\pi_{max} = \infty$, however, with real data, we can not integrate until infinite. Here we will use $\pi_{max} = 80 Mpc/h$. The result does not change when we change the upper limit of the integral for $\pi_{max} > 60 Mpc/h$ and large σ in the data.

Davis and Peebles [26] show that $\Xi(\sigma)$ is directly related to the real-space correlation function.

$$\Xi(\sigma) = 2 \int_{\sigma}^{\infty} \frac{r \xi(r) dr}{(r^2 - \sigma^2)^{\frac{1}{2}}}. \quad (20)$$

It is possible to estimate $\xi(r)$ by directly inverting $\Xi(\sigma)$ (Saunders et al. [27])

$$\xi(r) = -\frac{1}{\pi} \int_r^{\infty} \frac{(d\Xi(\sigma)/d\sigma)}{(\sigma^2 - r^2)^{\frac{1}{2}}} d\sigma. \quad (21)$$

Assuming a step function for $\Xi(\sigma) = \Xi_i$ in bins centered on σ_i , and interpolating between values,

$$\xi(r) = -\frac{1}{\pi} \sum_{j \geq i} \frac{\Xi_{j+1} - \Xi_j}{\sigma_{j+1} - \sigma_j} \ln \left(\frac{\sigma_{j+1} + \sqrt{\sigma_{j+1}^2 - \sigma_i^2}}{\sigma_j + \sqrt{\sigma_j^2 - \sigma_i^2}} \right) \quad (22)$$

for $r = \sigma_i$.

We take the redshift space anisotropic model $\xi(\sigma, \pi)$ in Eq.(14), with a fixed $\beta = 0.35$ and $\sigma_v = 400 \text{ km/s}$, and we use Eq.(19) to obtain the projected correlation function $\Xi(\sigma)$ as if it was data. We use different values to fix the upper limit in the integral: $\pi_{max} = 60 \text{ Mpc/h}$, 80 Mpc/h , 100 Mpc/h and 200 Mpc/h (dotted lines in top panel of Fig.1), and compare the "true" result obtained from Eq.(20) (solid line in top panel of Fig.1). As we increase π_{max} we approach the true result, but we can not integrate until 200 Mpc/h in real data because, as will be shown in the following sections, data is quite noisy for $\pi > 60 \text{ Mpc/h}$. The implication of these results is that we will not be able to recover the true values of $\Xi(\sigma)$ from $\xi(\pi, \sigma)$. But we can use this method at smaller scales (see Paper II).

In the bottom panel of Fig.1 we see the real-space correlation function recovered from the previously calculated projected correlation function with different π_{max} , Eq.(21). We obtain a good estimation of $\xi(r)$ below 30 Mpc/h , where we will study the non-linear bias (see Paper II).

This analysis has been done for different values of β and σ_v and we find very similar conclusions. For illustration, we have shown in our plots the values that are more in concordance with real LRG SDSS data.

Once we recover the real-space correlation function, we can also estimate the ratio of the redshift-space correlation function, $\xi(s)$, to the real-space correlation function, $\xi(r)$, which gives an estimate of the redshift distortion parameter, β , on large scales:

$$\frac{\xi(s)}{\xi(r)} = 1 + \frac{2\beta}{3} + \frac{\beta^2}{5}. \quad (23)$$

As we have shown in Fig.(1), $\xi(r)$ will be in general slightly overestimated at large scales when we estimate it from the projected correlation function $\Xi(\sigma)$, so the expression $\frac{\xi(s)}{\xi(r)}$ will in general be slightly lower than expected on large scales.

III. SIMULATIONS AND ERRORS

We first present the simulations used in this paper. Next we show how simulations have been used to provide an error estimate for the different statistics used in

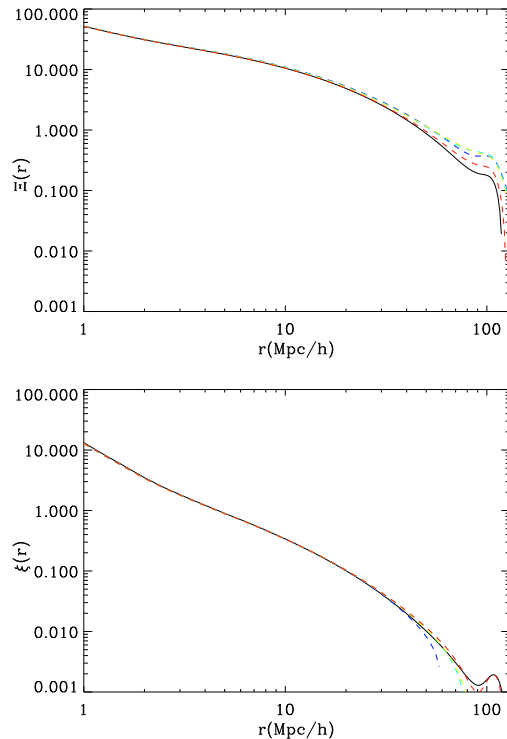


FIG. 1: *Top*: Solid line shows the projected perpendicular correlation function $\Xi(\sigma)$ calculated theoretically from $\xi(r)$ in Eq.19, for a model with $\beta = 0.35$ and $\sigma_v = 400 \text{ km/s}$. This is compared to integral of $\pi - \sigma$ in Eq.20 with $\pi_{max} = 60$. (cyan), 80 . (blue), 100 . (yellow), 200 . (red). *Bottom*: Estimation of the real space correlation function by deprojecting the dotted color lines of $\Xi(r)$ in the top panel using Eq.21. We can see good agreement up to scales of 30 Mpc/h .

this paper. Finally we use the simulations to validate the methods that we will later apply to real data. We will conclude that the methods and errors that we use to obtain parameters from LRG data are all well validated by simulations. We follow similar methodology and notation as in Cabré et al. [28].

A. Simulations

We have used different comoving outputs (between $z=0.0$ and $z=0.3$) of a MICE simulation, run in the supercomputer Mare Nostrum in Barcelona by MICE consortium (www.ice.cat/mice) in order to study the errors and validate the models used. The simulation contains 2048^3 dark matter particles, in a cube of side 7680 Mpc/h , $\Omega_M = 0.25$, $\Omega_b = 0.044$, $\sigma_8 = 0.8$, $n_s = 0.95$ and $h = 0.7$. We have divided this big cube in 3^3 cubes of side $2 \times 1275 \text{ Mpc/h}$, and taking the center of these secondary cubes as the observation point (as if we were at $z=0$), we apply the selection function of LRG, which arrives until $z=0.47$ ($r=1275 \text{ Mpc/h}$). We can obtain 8 octanes from the secondary sphere included in the cube, so at the

end we have 8 mock LRG catalogs from each secondary cube, which have the same density per pixel as LRG in order to have the same level of shot noise, and the area is slightly smaller (LRG occupies 1/7 of the sky with a different shape). The final number of M independent mock catalogs is 216 (27x8).

We use both dark matter particles and groups in this simulation. By definition, there is no bias in the dark matter particles, so $\beta = \frac{\Omega_m(z)^{0.55}}{b} = 0.62$, where $\Omega_m(z) = \Omega_m(1+z)^3 / (\Omega_m(1+z)^3 + 1 - \Omega_m)$ and $b = 1$. To simulate biasing we select groups of particles using friend-of-friends with linking scale of 0.20 (we have also used 0.16 with consistent results). At $z = 0$ we find a total of 107 million groups with more than 5 particles ($M > 1.87 \times 10^{13}$). These groups correspond to DM halos when the number of particles in the group is large [29]. We have also used a MICE simulations with 2048^3 dark matter particles, in a cube of side 3072Mpc/h (which we call MICE3072, same parameters as MICE7680) which has 15 times better mass resolution to check for mass resolution effects. We find very similar results in both cases to the extent that we can compare the smaller number statistics. When we select groups with $M > 2 - 4 \times 10^{13}$, both the clustering amplitude ($b_1 \simeq 1.9 - 2.2$ for $\sigma_8 = 0.8$) and the number density ($\bar{n} \simeq 4 - 6 \times 10^{-5}$) are similar to the real LRG galaxies in our SDSS sample (the range reflects the fact that the actual number depends on LRG sample used, ie redshift and selection). We have explored a number of cases to make sure we understand how errors depend on number density and bias. We will focus in presenting results for 3 different cases: a) dark matter particles at $z = 0.3$ ($b = 1$, $\beta = 0.62$), diluted to fit LRG number density b) groups with $M > 2.2 \times 10^{13}$ ($b = 1.9$, $\beta = 0.25$) at $z = 0$, c) groups with $M > 3.74 \times 10^{13}$ ($b = 3$, $\beta = 0.23$) at $z = 0.5$, which expand the range b , β , z and densities in the real LRG in our samples.

We generate the mock catalogs applying redshift distortions in the line-of-sight direction,

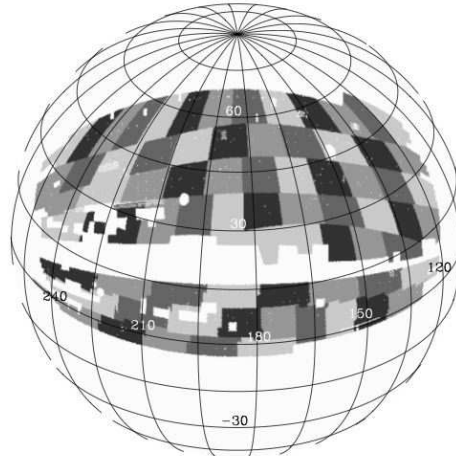
$$s = r + v_r/H(z)/a(z) \quad (24)$$

We obtain the Monte Carlo (MC) error from the dispersion of M independent realizations of our universe. For M realizations, the MC covariance is

$$C_{ij} = \frac{1}{M} \sum_{k=1}^M (\xi(i)^k - \hat{\xi}(i))(\xi(j)^k - \hat{\xi}(j)) \quad (25)$$

where $\xi(i)^k$ is the measure in the k -th simulation ($k=1, \dots, M$) and $\hat{\xi}(i)$ is the mean over M realizations. The case $i=j$ gives the diagonal error (variance). Typically, we need $M = 100$ independent simulations for the diagonal error, and more for the covariance matrix, depending on the case. The MC error is an estimation of the true error, but it takes lots of computational time and it also requires simulations with the same particularities of the

JK zones in DR6 catalogue



JK zones in the mock catalogue

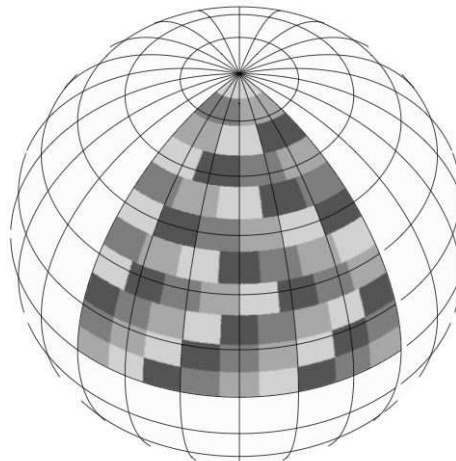


FIG. 2: Top panel: JK zones for the LRG catalog (equatorial coordinates). Bottom panel: the mock catalog with its JK zones

data analyzed. When we refer to off-diagonal elements of C_{ij} we use the normalized covariance:

$$\hat{C}_{ij} \equiv \frac{C_{ij}}{\sqrt{C_{ii}C_{jj}}} \quad (26)$$

which ranges from -1 to +1. Values of $|\hat{C}_{ij}| < 0.2$ usually have little impact on the error analysis.

In the case of the jackknife (JK) error, we obtain the different realizations that we need to compute the error from the same data (or from a single realization in the case of simulations). This is done by dividing the sample in M zones. Each JK subsample consists in the whole catalog except from one of these M zones. In this case, as the realizations are clearly not independent, we apply a multiplicative factor of $(M - 1)$ the previous covariance to account for this effect. Fig.2 shows the octane catalog used for the galaxy mocks divided in 63 jackknives zones,

with similar area and shape; and the SDSS DR6 real catalog divided in 73 jackknife zones. We have tested that the difference in mask does not make a large difference in the error analysis.

We next use the dark matter and group mock simulations to probe the limit of the JK errors, which we want to use in LRG data, We study the errors in the redshift space correlation function $\xi(\pi, \sigma)$, the monopole $\xi(s)$ and the quadrupole $Q(s)$. Finally, we use the simulations to validate the models that we will use with real data.

B. Errors in $\xi(\sigma, \pi)$

We study here the errors in the anisotropic redshift-space correlation function $\xi(\sigma, \pi)$. The JK and MC errors only seem to agree at small perpendicular scales $\sigma < 20 \text{ Mpc}/h$, which means that we can not use the JK error for large σ values. This is illustrated in Fig.3. The reason for this behaviour could partially be related to the fact that we have defined the JK zones in angular space, ie in the σ direction. When σ is large, the different JK zones are not independent. This could explain why JK errors do not work so well. In the radial direction, the different JK zones are more independent from each other and the JK errors give a better agreement to MC errors.

1. Error model

We have found a phenomenological model (we sometimes call it "theory" or "analytical" error) for the errors that match well the MC errors at large σ , even at large scales. The advantage of using a model is that is smoother than MC errors and can also be used to calibrate JK errors. We will first test this model in different situations.

Our "theory error" has a dominant shot-noise contribution, which scales as $1/\sqrt{\text{number of pairs}}$, and a part proportional to the signal. This works well in this case because our LRG sample is shot-noise dominated, specially at large scales, and we are able to separate both contributions, as if we were in a diagonal space. In general, the analytical derivation of the error is more complicated than this simple modelling. We propose the error to have the following form $\Delta\xi = \Delta\xi_{\text{shot-noise}} + \Delta\xi_{\text{signal}}$, with two arbitrary coefficients α_{noise} and α_{signal} , so that:

$$\Delta\xi = \alpha_{\text{noise}} \Delta\xi_{\text{Poisson}} + \alpha_{\text{signal}} \xi \quad (27)$$

adding these two terms linearly fits the simulations better than in quadrature. For Poisson shot-noise we have by definition that $\alpha_{\text{noise}} = 1$. This works very well for dark matter mocks, but we will show that groups do not follow the Poisson distribution and $\alpha_{\text{noise}} = 1.4$. We can associate α_{signal} to the number of independent nodes in

the catalog and we therefore expect α_{signal} to scale with the square root of the volume of the sample used. We also expect α_{signal} to depend on the binning used. We use the ξ estimator of Landy and Szalay [30] to calculate the correlation function,

$$\xi(\sigma, \pi) = \frac{DD - 2DR + RR}{RR} \quad (28)$$

In the case of dark matter mocks, the error that comes from having a limited number of data-data (DD) pairs (Poisson shot-noise) is: $\text{err}(DD) = 1/\sqrt{RR/N_R^2}$, and for DR pairs: $\text{err}(DR) = 2/\sqrt{RR/N_R}$, where the random catalog is N_R times denser than the data catalog. The error in random-random is insignificant, because we are using a denser random catalog. We add the different errors in quadrature to find:

$$\Delta\xi_{\text{Poisson}} = \sqrt{\frac{N_R^2 + 4N_R}{RR}} \quad (29)$$

We can reduce the error in $\xi(\pi, \sigma)$ by increasing the number of particles in the random catalog, modifying the error coming from DR, which is inversely proportional to the square root of the pairs data-random. The first part of the error is always the same, because it depends only on the data. For $N_R = 10$, as in the simulations, $\Delta\xi_{\text{Poisson}} = \sqrt{140./RR}$, so the DR part is a 40% of the DD part. For $N_R = 20$, as in the analysis of LRGs, $\Delta\xi_{\text{Poisson}} = \sqrt{480./RR}$, so the DR part is now a 20% of the DD part. For a binning of 5Mpc/h, we find $\alpha_{\text{signal}} = 1/95$ and for binning of 1Mpc/h, $\alpha_{\text{signal}} = 1/25$. At large $\sigma > 20 \text{ Mpc}/h$, the signal part in $\xi(\pi, \sigma)$ is not very significant. This can be seen in Fig.3, where the linear dashed line correspond to the shot-noise term and the curved dashed line (only important on scales $\pi < 20 \text{ Mpc}/h$) also includes the signal part in Eq.27. For small σ scales, JK and MC coincide so we can just use JK error from the actual LRG data. In practice we prefer to use our model error to the JK error because this avoids introducing noise in the error analysis, but we have checked that none of our results depends on this choice.

2. Super-Poisson errors

In the case of groups, the Poisson model for the shot-noise does not work well. The reason for this is that groups are selected using friend-of-friends with linking length of $r = 0.20$ times the interparticle separation. This means that groups create excluding regions where we can not randomly locate another group and therefore do not follow a Poisson distribution [31]. Shot-noise is larger in this case, which we call "super-Poisson". After exclusion, the fraction of available volume is $(1-r)^3 \simeq 0.5$ so we expect the Poisson term to be

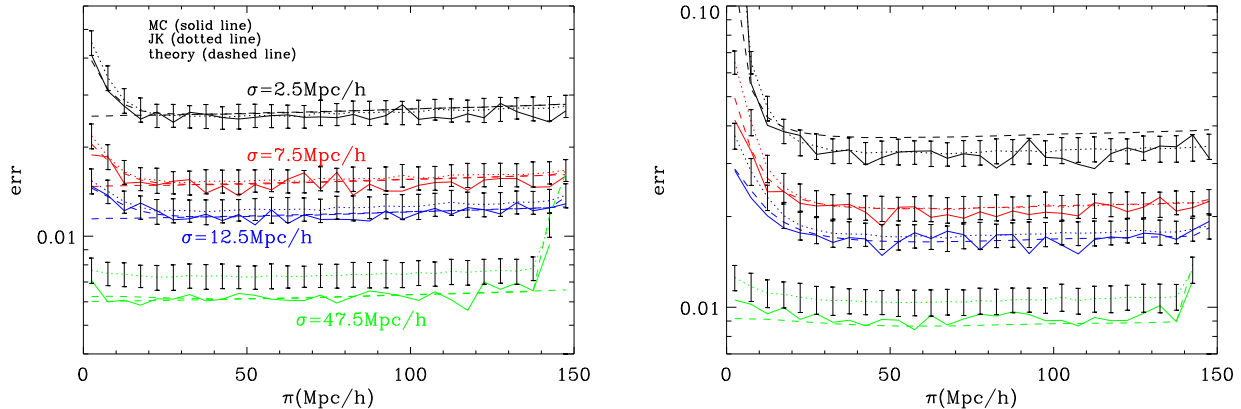


FIG. 3: We compare different error estimators for the 2-point correlation function in redshift space $\xi(\sigma, \pi)$ for MICE dark matter mocks (left panel) and group mocks with $b = 1.9$ (right panel). We fix the perpendicular distance σ and move along the line-of-sight π as indicated in the figure. The errors are: MC (solid line), theory (dashed line) with and without the signal part of the error, and JK (dotted line with errorbars). As we move to higher σ (lower amplitudes), JK starts to fail, but the analytical and MC errors always agree well. On the radial direction, top lines for $\sigma = 2.5\text{Mpc}/h$, the JK and MC agree well, but theory model only works in the dark matter case.

corrected by the square root of this fraction, ie roughly $\alpha_{noise} \simeq 1/(1-r)^{3/2} \simeq 1.4$. This is exactly what we find for our model in Eq.27 for group mocks. What about real LRG galaxies? Do they follow the Poisson shot-noise or the groups shot-noise model? Real LRG data seems to follow more closely the group shot-noise as we find that we need $\alpha_{noise} = 1.4$ rather than $\alpha_{noise} = 1$ for Poisson term when we fit the JK errors in the real data at small σ . As we have seen with mocks, the JK errors reproduce very well the true errors for small σ both the Poisson (dark matter) and super-Poisson (groups). The amplitude of the JK errors on small σ is quite closer to group mocks than to dark matter mocks (this can be seen by comparing Fig.4 to Fig.5 below). This by itself is a very interesting result because it clearly shows that LRG galaxies have a tendency for exclusion. This suggest that a dominant fraction of LRG populate separate dark matter halos. It also shows that using dark matter mocks or a standard (Poisson) point process to simulate LRG will result in an important underestimation of errors.

3. Errors in LRG

Fig.4 shows the full 2D version of Fig.3. We show here the differences in the diagonal error between MC, JK and the theory error in Eq.27, when binning the correlation function with $5\text{Mpc}/h$. MC error is calculated using MICE simulation and JK is the mean over all the JK that we have calculated in each mock. JK errors work well for small $\sigma < 20\text{Mpc}/h$ but that become higher than MC when going to large σ for the reasons explained above. Our "theory" error model form agrees with MC error at all scales, except in the radial direction, $\sigma = 2.5\text{Mpc}/h$, for the case of group mocks (where

we used a fixed $\alpha_{noise} = 1.4$ at all σ), which is slightly higher than the MC or the JK errors. The model for dark matter mocks, with $\alpha_{noise} = 1$ does well at all σ . This can be seen in Fig.3. Thus in the radial direction we need to change α_{noise} for groups to $\alpha_{noise} = 1.2$, a lower value than $\alpha_{noise} = 1.4$. The reason for this is most probably the random component of peculiar velocities in redshift space, which randomizes the radial positions of group and reduces the super-Poisson shot-noise contribution, which comes from self-exclusion in group positions. This is no problem when analyzing real data as we can fit α_{noise} to match the JK error at small values of σ (with a different value at $\sigma < 5$ than at $5 < \sigma < 20\text{Mpc}/h$) and then use our error model for large values of σ where JK does not work well. We could also directly use the MC errors in the group mocks, which seem to agree quite well with real LRG data (ie JK errors are very similar in both cases, see Fig.5).

In Fig.5 we show the JK error obtained from the real LRG data using a random catalog 10 times denser than the data (as done with the mocks), and the analytical form with a fixed $\alpha_{noise} = 1.4$ and $\alpha_{signal} = 1/95$. As in the mocks, for large σ the JK error is bigger than the analytical error, which should be more representative of the true (MC) error. At small scales the model follows the JK prediction, except for $\sigma < 5\text{Mpc}/h$ where we need to change to $\alpha_{noise} = 1.2$ (the figure shows the model for $\alpha_{noise} = 1.4$ at all σ). Note the similarity between the errors in the data and in the group mocks in Fig.4. For our final analysis of the data we use a random catalog 20 times denser to reduce the error contribution due to the shot-noise in the randoms.

We have done a similar analysis with the L-BASICC halo simulations from Durham, which have approximately the same bias as real LRG in SDSS, and we find

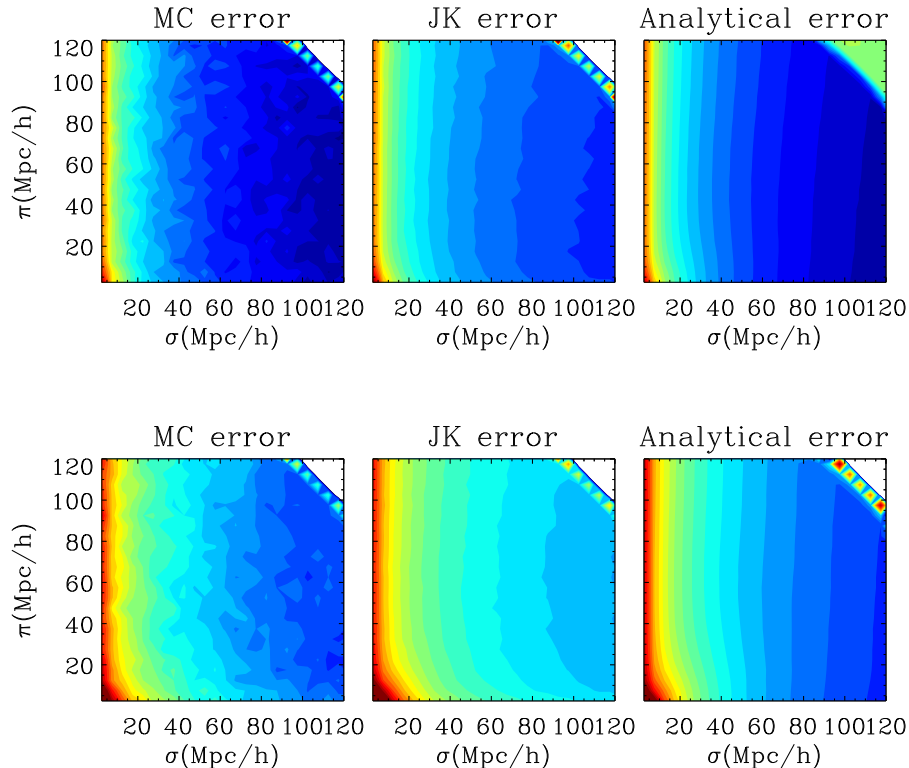


FIG. 4: Diagonal error in $\xi(\sigma, \pi)$ in redshift space for MICE dark matter simulations (top panel) and groups with $b = 1.9$ (bottom panel) with contours $\xi = 0.0035 - 0.05$ (log increment=0.1)

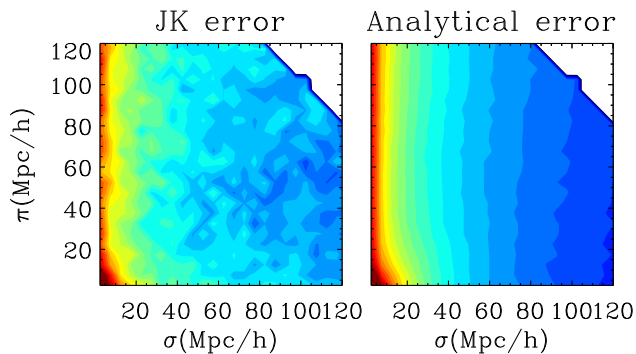


FIG. 5: Same as Fig.4 for real LRG data.

very good agreement with our fitting formula. If we use a random catalog 20 times denser, as we do for the analysis of the data, the error is lower, just as expected.

4. Covariance $\xi(\pi, \sigma)$

So far we have shown diagonal errors. The normalized covariance is in fact quite small for dark matter mocks. It has the same approximate shape and amplitude for all the points. The amplitude of the covariance is just given by the distance between bins: at a separation of $5\text{Mpc}/h$ the normalized covariance is ≤ 0.1 . This is also true for group mocks in the radial direction. But the covariance is larger in the case of groups for $\sigma > 5\text{Mpc}/h$. At a radial distance of $5\text{Mpc}/h$ between bins in $\xi(\pi, \sigma)$ the normalized covariance is about 0.5 and dies below 0.2 for bins separated by more than $15\text{Mpc}/h$. This is illustrated in Fig.6, which just shows the covariance in one of the bins. Other cases are very similar. The inner contour, which corresponds to 0.5 for groups, is very similar in shape for dark matter and radial bins, but the amplitude in this case is 0.1.

If we bin the plane $\pi - \sigma$ with $1\text{Mpc}/h$, the same theory error form in Eq.27 still works on all scales. So does the JK, at low σ . But in general errors are higher than when using a wider bin (smaller bin means smaller number of pairs). This increase is compensated by a decrease in the covariance, which becomes practically zero for all elements outside the diagonal.

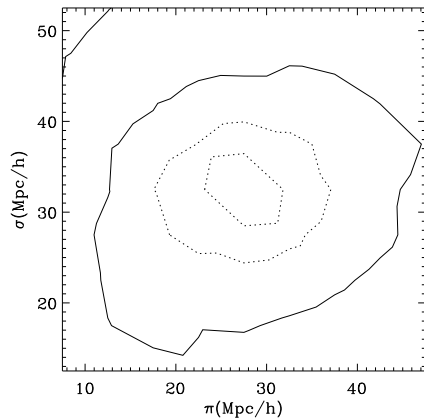


FIG. 6: Normalized covariance of $\xi(\pi, \sigma)$ for groups in a bin centered at position ($\sigma = 32, \pi = 28$). Contours show fix values of the covariance away from the central position, with contours 0.5, 0.3, 0.2 and 0.1.

C. Errors in the monopole $\xi(s)$

The error in the monopole is not easy to predict theoretically, but in this case JK error works very well for both variance and covariance on all scales. In the left panel of Fig.7 we plot the monopole when we bin the data with a separation 5Mpc/h: black for the dark matter mocks and red for LRG data (which will be presented in more detail in next section). At the right panel, we see the difference between the mean JK error and its dispersion (solid line with errors) and the MC error (dashed line), and over-plotted the JK error for the real LRG (color). As can be seen, the error for LRG is larger than the one in simulations, since the signal is also higher, due to an overall bias b in the amplitude. The small difference between blue and red line in Fig.7 is due to the number of the particles in the random catalog (N_R), which does not change the estimation of the error in this case. Results are very similar for group mocks, with higher amplitudes, as expected. The important point here is that the JK error works well at all scales.

The normalized covariance, in Eq.26, for the monopole is plotted in Fig.8. The result is not completely smooth for the MC case (top panel), because we need more than 216 simulations to have a smooth result. But we see that it has the same shape than JK covariance, which we will use to fit our LRG data. JK covariance is smoother than the MC because we have taken the mean over 216 x 63 realizations (216 mocks x 63 JK zones), which seems enough to converge. The bottom panel shows JK errors in the real LRG data, which is quite similar to the mocks, but looks noisier because this is just a single realization.

We have also binned the monopole $\xi(s)$ with 1Mpc/h. JK error also works in this case, and we also see that the error is higher here than in the 5Mpc/h bin, while the covariance is smaller, practically equal to zero.

D. Error in the quadrupole $Q(s)$

For the quadrupole, the JK error also works quite well, as we can see in Fig.9 for 5Mpc/h (top panels) and 1Mpc/h binning (bottom panels). Again here, the solid line with errors shows the JK error and its dispersion, the dotted line is the MC error, and the color and lower line is the JK error in LRG data. The error for LRG data, in the quadrupole, is lower than the simulations one. This is because the error here is proportional to the signal, and in this case, LRG signal is lower since $Q(s)$ depends on β which depends inversely on bias b . Results for group mocks are in good agreement with data and yield similar results for the comparison on JK and MC errors.

E. Validity of the models

We also use the simulations to test the methods that we will apply to real data (LRG) in the following sections. We want to study if we can recover the parameters that were input in the simulations.

1. Recovering the real-space correlation function

We first estimate the 2-point real-space $\xi(r)$ and redshift-space $\xi(s)$ correlation functions and compare then to the input model that describes the simulation. We find very good agreement. We look at the ratio $\xi(s)/\xi(r)$ between the redshift space and real space, which should be a function of the distortion parameter β at large scales (and for the distant observer approximation), as in Eq.(23). In Fig.10 we have plotted the mean ratio over the simulated mocks, with its error, and over-plotted in red the expected value for the ratio at $\beta = 0.62$ as in the input model. It seems to converge above 10Mpc/h, which is in agreement with other analysis (see Fig.13 in Hawkins et al. [32]). We could obtain β from the ratio $\xi(s)/\xi(r)$, but it is difficult in real data since we do not have direct information of the real-space $\xi(r)$, only through integration of the anisotropic $\xi(\sigma, \pi)$ through the line-of-sight (see §II C). The advantage of using this ratio is that it converges to a constant value at small scales. But we can only use this below 30 Mpc/h with real data because the recovered real-space correlation function $\xi(r)$ starts to fail on larger scales (see Fig.1). We have fitted these scales with the simulations and the results for β are the ones expected. However, we have checked that it is better to obtain β from the quadrupole $Q(s)$, since it is more independent of other cosmological parameters and can be trusted to larger scales.

2. Fitting of the quadrupole $Q(s)$ to obtain β and σ_v

We can calculate the multipoles of $\xi(\pi, \sigma)$ to decompose the anisotropy between the LOS and the perpen-

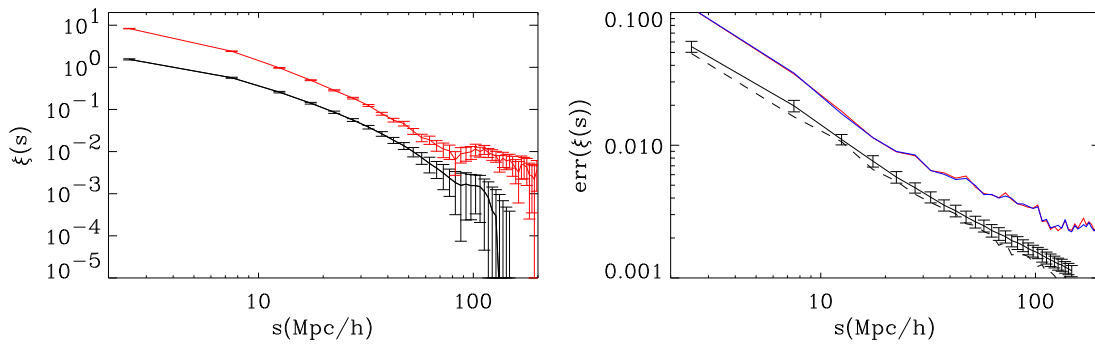


FIG. 7: Left: Monopole $\xi(s)$ with errors for MICE simulations (black, lower line) and for real LRG (red, upper line) using a bin of 5Mpc/h. Right: Diagonal error for MICE dark matter simulations (JK with dispersion solid black line, MC dashed black line) and for JK errors in real LRG data (red for $N_R = 10$ and blue for $N_R = 20$)

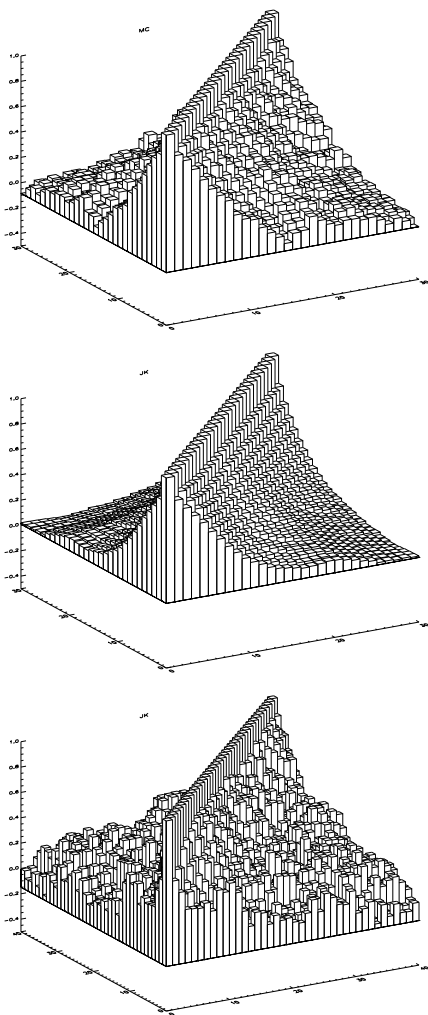


FIG. 8: Normalized covariance of MC (top) and JK (middle) for the monopole $\xi(s)$ in MICE group mocks (for binning of 5Mpc/h). Bottom panel correspond to JK error in the real LRG data

dicular direction. We have tested with models that the monopole $\xi(s)$ and quadrupole $\xi_2(s)$ and even the combination $\xi_2(s)/\xi(s)$ depend strongly not only on β and σ_v , but also on other parameters like the shape of the correlation function (ie Ω_m , Ω_b and n_s), the non-linear bias and the overall amplitude. On the contrary, the reduced quadrupole $Q(s)$, defined in Eq.(17) only depends strongly on σ_v and β , but not on the bias. So when using the quadrupole we do not need an expression for the non-linear bias or a prior on Ω_m (the shape of $\xi(r)$) to extract the β information. We can fix these parameters, and only change β and σ_v . The asymptotic value of $Q(s)$ for large scales in Eq.(18) is a function of β , but it is always biased to higher values because of the random velocities. So it is dangerous to obtain β from this asymptotic approximation. We instead generate our model for $Q(s)$ based on the multipoles of $\xi(\sigma, \pi)$ in Eq.(16) and Eq.(17).

For the dark matter mocks we have that $\beta = 0.62$ (see §III) and σ_v is approximately 400km/s on large scales, but higher when approach scales smaller than 10 Mpc/h (see Fig.11). We fit the quadrupole obtained for each mock separately. The mean over all the mocks gives the correct exact value of $\beta = 0.62$ and a value of $\sigma_v \simeq 450\text{Km/s}$ which is slightly larger than the asymptotic large scale value of 400 Km/s. This is probably because we are obtaining an effective σ_v which also accounts for the values at lower scales which are larger, as shown in Fig.11. At $1 - \sigma$ (2 dof) $\sigma_v \simeq 450\text{Km/s}$ is consistent with the asymptotic value at large scales, which is plotted as a red dot in Fig.12. In Paper-II of this series we show how to find the exact value for σ_v as a function of scale.

In the top panel in Fig.12, we show the mean contour $\beta - \sigma_v$ which is the average over the individual contours in each simulation, obtained from $Q(s)$. In the bottom panel, we show the best fit model over-plotted over the mean $Q(s)$ with the MC errors. The MC errors here correspond to a single mock, while errors in the mean value are \sqrt{N} times smaller ($N=216$ in our simulations). In the bottom panel of Fig.12, we plot the errors corresponding to a single mock. We find similar results for group mocks,

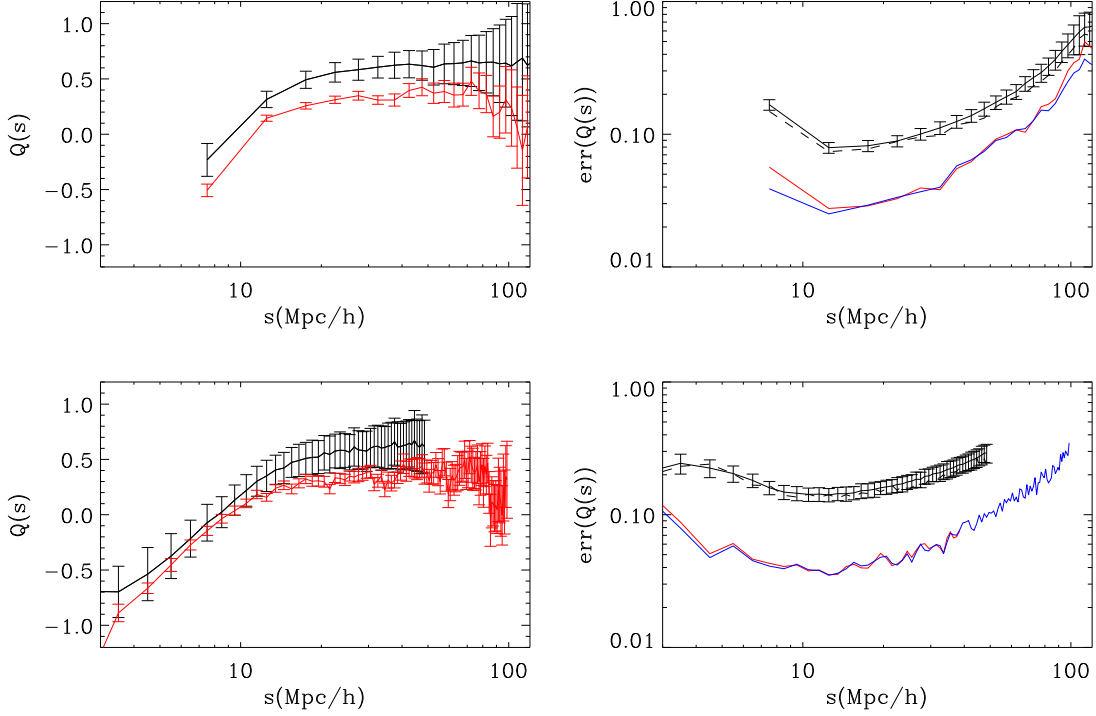


FIG. 9: *Top Left*: $Q(s)$ with errors for MICE dark matter mocks (black higher signal) and for LRG (red lower signal) using a bin of 5Mpc/h. *Top Right*: Diagonal error for MICE simulations (JK with dispersion solid black line, MC dotted black line) and for LRG data (red and blue for $N_R = 10$ and $N_R = 20$). *Bottom*: Same as top with a bin of 1Mpc/h.

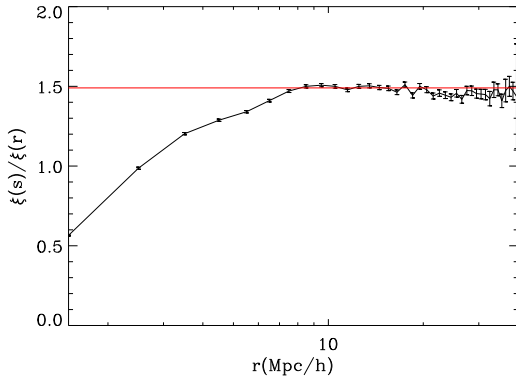


FIG. 10: Mean $\xi(r)/\xi(s)$ over MICE dark matter mocks with errors (on the mean, scaled as $1/\sqrt{nsim}$), and Kaiser prediction for large scales for $\beta = 0.62$, corresponding to the input model (red)

which have different values of β . We conclude that the model used for the quadrupole, assuming a constant σ_v , is perfect to obtain β and an effective σ_v which does not have to correspond necessarily to the large scale value, but rather to a combination of σ_v at different scales.

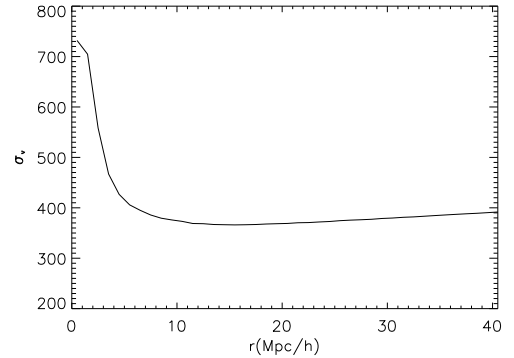


FIG. 11: Dispersion in the pairwise velocity distribution σ_v in the MICE simulation as described in Eq.(15) when we change the distance between particles

3. Fitting of large scales: Ω_m and amplitude

From large scales, we will obtain the shape of the linear correlation function $\xi(\pi, \sigma)$. Here we will only fit Ω_m and the amplitude of the correlation. We have fixed n_s , Ω_b and h to the values found in recent results of WMAP, SNIa and previous LSS analysis.

As we have seen in §II C we can not rely on the projected correlation function at large scales, or the recov-

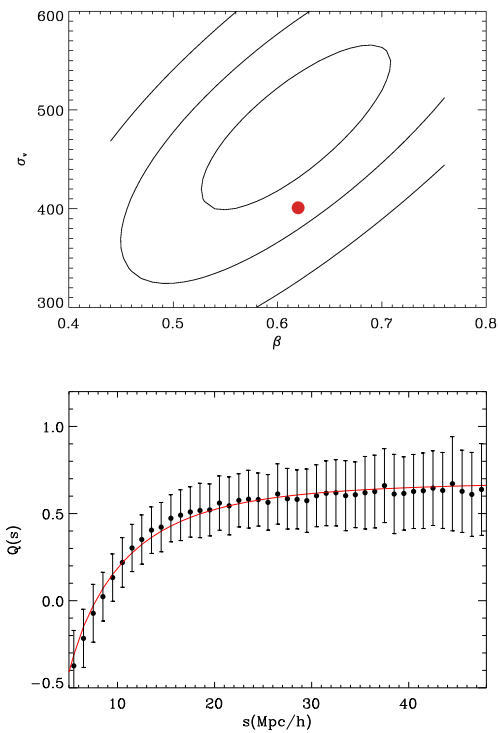


FIG. 12: *Top panel:* Mean best fit $\beta - \sigma_v$ to MICE quadrupole $Q(s)$. The red dot shows the value for the input β and σ_v at large scales. Contours are $\Delta\chi^2 = 1, 4$ and 9 using MC errors for a single mock. *Bottom panel:* $Q(s)$ with MC errors (points), and best model (red). We recover the input $\beta = 0.62$, but σ_v is slightly biased to higher values, probably because we are obtaining an effective σ_v which also accounts for the values at lower scales.

ered real space correlation function, so the only way to extract information about the shape of the real space correlation function using the same data is from $\xi(\sigma, \pi)$. We use models that vary with Ω_m , linear amplitude, σ_v and β . The linear amplitude Amp refers to the factor $b(z)\sigma_8$, where $b(z)$ is the bias at redshift z . $b(z)$ and σ_8 are completely degenerated in the correlation function, also with the growth factor $D(z)$. In fact, what we obtain from observations is $b(z)\sigma_8D(z)$, but $D(z)$ is known for each cosmology and the median redshift of the slice. We prove using simulations that we can use linear bias and the σ_v and β found using the quadrupole. The best place to fit Ω_m and Amp , so that is independent on scale, is for intermediate scales, from $20\text{Mpc}/h$ to $60\text{Mpc}/h$, to be safe from non-linear bias. We also stay away from the line-of-sight (LOS) where fingers of God can alter the information. We cut an angle of $30\text{-}40$ deg away from the LOS. We marginalize over $\beta - \sigma_v$ and obtain a contour for $\Omega_m - Amp$ which is in very concordance with the input values. Although σ_v obtained from $Q(s)$ is just an effective value, simulations show that we recover the correct value of Ω_m . We can understand it, because σ_v does not play an important role in our selected range of scales

in $\xi(\sigma, \pi)$. If we extend to larger distances, the value for Ω_m is biased slightly to lower values, probably because of the wide angle effect. This is important for an angle of 10 deg between galaxies (see Matsubara [33]), which is more than $70\text{Mpc}/h$ for our worst case ($z=0.15$), in the perpendicular direction σ .

4. Model for the 2-point correlation function $\xi(\sigma, \pi)$

Finally, in Fig.13, we plot $\xi(\sigma, \pi)$ at large scales for the mean over MICE mocks (colors). We over-plot in solid lines the best model (using Eq.(14)). In all cases, we use an effective $\sigma_v = 400\text{km}/s$. Note that we use square bins (pixels) of $5\text{Mpc}/h$ side at all scales and this dilutes the FOG at small σ . The model works very well compare to simulations. The overall amplitude is quite different in each case, but the shape is also quite different. The larger the value of β the greater squashing effect in the radial (π) direction. Also note the closed contours in the radial direction between $\pi = 50 - 100$ Mpc/h (in dark blue). They correspond to a region of negative amplitude caused by the squashing (Kaiser) effect. The larger the value of β the larger the region with negative values. This region is surrounded by the BAO ring at about 100 Mpc/h. It is remarkable how well this is followed by simulations, which indicates that this is a very significant feature. We will show below that data also follows this feature.

Simulations also show a good agreement with the BAO peak, including some detection in the radial direction which is enhanced by noise. This will be studied in more detail in Paper IV of this series.

We see that the obtained correlation (colored) differs slightly from the distant observer approximation theory (lines) at large σ and $\pi \simeq 0$. The redshift space correlation distortion in real surveys, which are not located at infinite, depends on π and σ , but also on the angle between galaxies θ and the angle γ_z between the direction LOS (at $\theta/2$) and the vector which goes from galaxy 1 to galaxy 2 (following the notation used in Matsubara [33]). In the distant observer approximation we assign to the angle between galaxies the value $\theta = 0$. Matsubara [33] has studied the differences between the real correlation and the approximation for distant observers. In general, the approximation is good for angles θ below 10 deg, which include all the zone we are using for our analysis in LRG data (the worst case comes from the closest galaxies at $z=0.15$, where $\sigma \simeq 80\text{Mpc}/h$ corresponds to $\theta = 10\text{deg}$). The correlation also depends on the γ_z angle. We can see in Fig.9 of Matsubara [33] a comparison between the real correlation, which depends on the distance between galaxies and both angles described above, and the distant observer correlation function, used in this work, which depends only on π and σ . Each position in the 2 dimensional $\pi - \sigma$ is a mixing of different θ and γ_z , because there is a range in redshift, but we can explain qualitatively the lack of power of the observed correlation respect to the distant observer approximation theory at

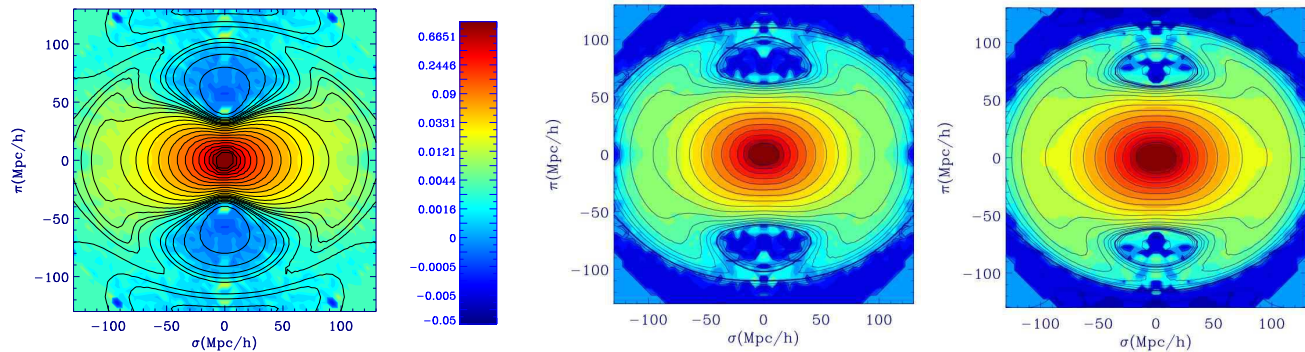


FIG. 13: Correlation function $\xi(\pi, \sigma)$ in different simulations: MICE dark matter mocks with $b = 1$ and $\beta = 0.63$ (left); group mocks with $b = 1.9$ and $\beta = 0.25$ (middle); and group mocks with $b = 3.0$ and $\beta = 0.23$ (right). The contour colors are from the simulations. We have overplotted in solid lines the corresponding levels for models with the same input parameters as the simulation in each case.

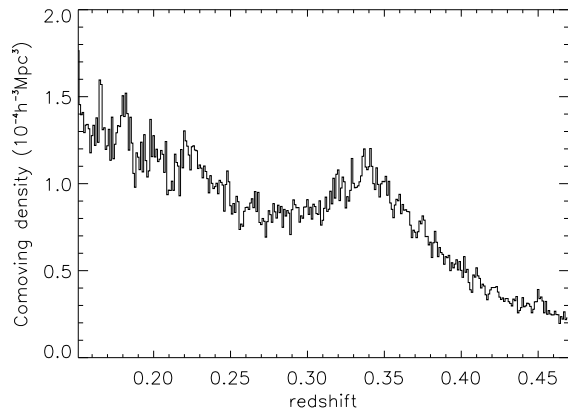


FIG. 14: Comoving density vs redshift for our selected LRGs

large σ and $\pi \simeq 0$.

We have also calculated the correlation function limiting the angle between galaxies to see in practice how $\xi(\pi, \sigma)$ is affected by wide angle effects. As we increase the restriction, we see how the σ direction recovers power in better agreement with the model predictions. In real data, we rather use all pairs given that this is quite a small distortion.

IV. THE DATA

The luminous red galaxies (LRGs) are selected by color and magnitude to obtain intrinsically red galaxies in Sloan Digital Sky Survey (SDSS). See Eisenstein et al. [34] or <http://www.sdss.org> for a complete description of the color cuts. These galaxies trace a big volume, around $1Gpc^3h^{-3}$, which make them perfect to study large scale clustering. LRGs are supposed to be red old elliptical galaxies, which are usually passive galaxies, with relatively low star formation rate. They have steeper slopes

in the correlation function than the rest of galaxies, since they reside in the centers of big halos, inducing non-linear bias dependent on scale, for small scales. They are well known galaxies, so they represent a good chance to use it as dark matter clustering tracers.

LRG's are targeted in the photometric catalog, via cuts in the (g-r, r-i, r) color-color-magnitude cube. Note that all colors are measured using model magnitudes, and all quantities are corrected for Galactic extinction following [35]. The galaxy model colors are rotated first to a basis that is aligned with the galaxy locus in the (g-r, r-i) plane according to:

$$\begin{aligned} c_{\perp} &= (r-i) - (g-r)/4 - 0.18 \\ c_{\parallel} &= 0.7(g-r) + 1.2[(r-i) - 0.18] \end{aligned}$$

Because the 4000 Angstrom break moves from the g band to the r band at a redshift $z \simeq 0.4$, two separate sets of selection criteria are needed to target LRGs below and above that redshift:

$$\begin{aligned} \text{Cut I for } z < 0.4 \\ r_{\text{Petro}} &< 13.1 + c_{\parallel} / 0.3 \\ r_{\text{Petro}} &< 19.2 \\ |c_{\perp}| &< 0.2 \\ m_{u50} &< 24.2 \text{ mag arcsec}^{-2} \\ r_{\text{PSF}} - r_{\text{model}} &> 0.3 \end{aligned}$$

$$\begin{aligned} \text{Cut II for } z > 0.4 \\ r_{\text{Petro}} &< 19.5 \\ |c_{\perp}| &> 0.45 - (g-r)/6 \\ g-r &> 1.30 + 0.25(r-i) \\ m_{u50} &< 24.2 \text{ mag arcsec}^{-2} \\ r_{\text{PSF}} - r_{\text{model}} &> 0.5 \end{aligned}$$

Cut I selection results in an approximately volume-limited LRG sample to $z=0.38$, with additional galaxies to $z \simeq 0.45$. Cut II selection adds yet more luminous red galaxies to $z \simeq 0.55$. The two cuts together result in about 12 LRG targets per deg^2 that are not already in

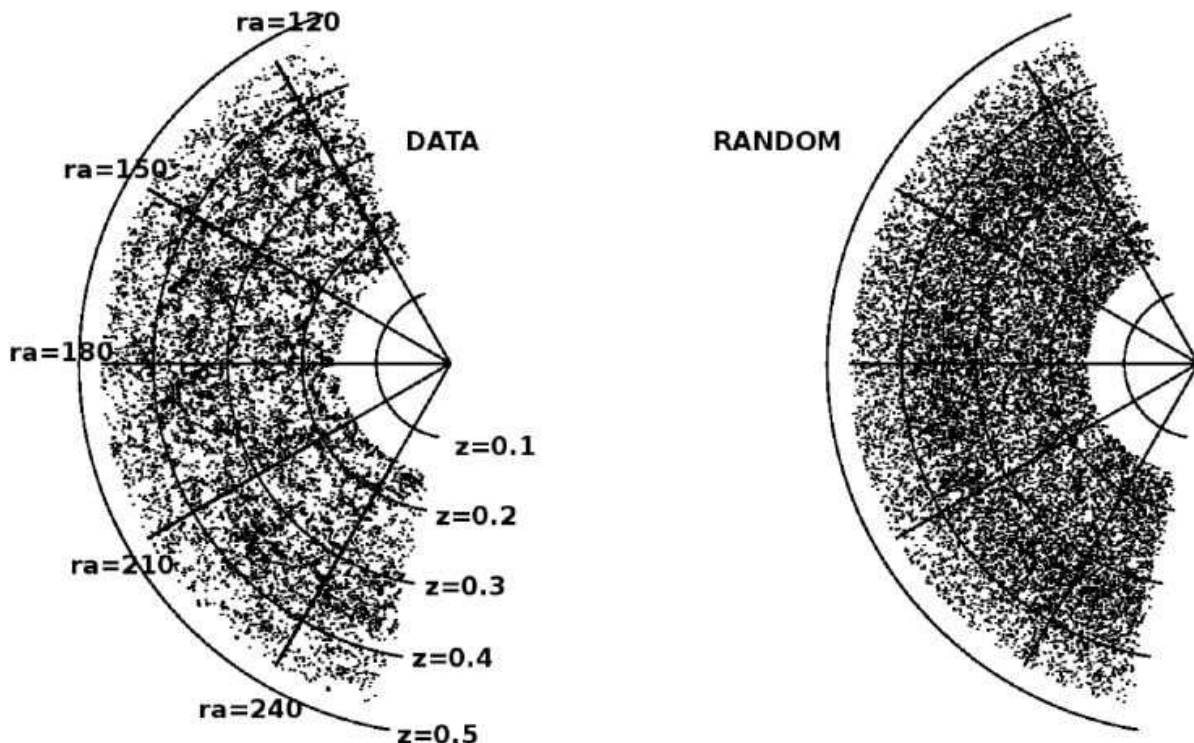


FIG. 15: Slice in dec = 32-40 deg showing ra vs redshift, in order to see the structure of the data (left panel). We also plot the random distribution for this slice (right panel)

the main galaxy sample (about 10 in Cut I, 2 in Cut II). The radial distribution and magnitude-redshift diagrams are plotted in Fig.32 and Fig.43.

We k-correct the r magnitude using the Blanton program 'kcorrect' [58]. We need to k-correct the magnitudes in order to obtain the absolute magnitudes and eliminate the brightest and dimmest galaxies. We have seen that the previous cuts limit the intrinsic luminosity to a range $-23.2 < M_r < -21.2$, and we only eliminate from the catalog some few galaxies that lay out of the limits. Once we have eliminated these extreme galaxies, we still do not have a volume limited sample at high redshift but we will account for this using a random catalog with identical selection function.

We show the comoving density in Fig.14 once we have removed the brightest and dimmest galaxies, and in Fig.15 we show the redshift space distribution in a slice of dec = 32-40 deg. We compare it with the same slice of random points. We see clear evidence of clustering in the data.

We have masked the catalog using at the first step the photometric DR6 mask, based on the number of galaxies per pixel. In previous works [28] we showed that the mask that we obtain statistically by dropping out the pixels with small number of galaxies gives identical correlation function that the one obtained by extracting the polygons masked by the SDSS team. After that, we compare our masked catalog to the LRG spectroscopic catalog, and we extract the galaxies that lay outside from the “good”

plates. Fig.40 illustrates the result.

Our mask could imprint spurious effects at very small scales. But we are not interested in such small scales, because fiber collisions in the redshift catalog are limiting our analysis. This is for distances less than 55arc sec, ie less than 0.3Mpc/h at the mean redshift of LRG data, $z=0.34$. We obtain 75,000 galaxies for the final catalog, from $z=0.15$ to $z=0.47$, ie over one cubic Gigaparsec (Gpc^3/h^3).

V. RESULTS

Here we define the parameters that we assume during all this work, which are motivated by recent results of WMAP, SNIa and previous LSS analysis: $n_s = 0.98$, $\Omega_b = 0.045$, $h = 0.72$. We will use the power spectrum analytical form for dark matter by Eisenstein and Hu [36], and the non-linear fit to halo theory by Smith et al. [37]. For part of our analysis we have followed the method explained in Hawkins et al. [32], an extensive analysis of redshift distortions in the 2dF catalog.

To estimate the correlation $\xi(\sigma, \pi)$, we use the ξ estimator of Landy and Szalay [30],

$$\xi(\sigma, \pi) = \frac{DD - 2DR + RR}{RR} \quad (30)$$

with a random catalog $N_R = 20$ times denser than the

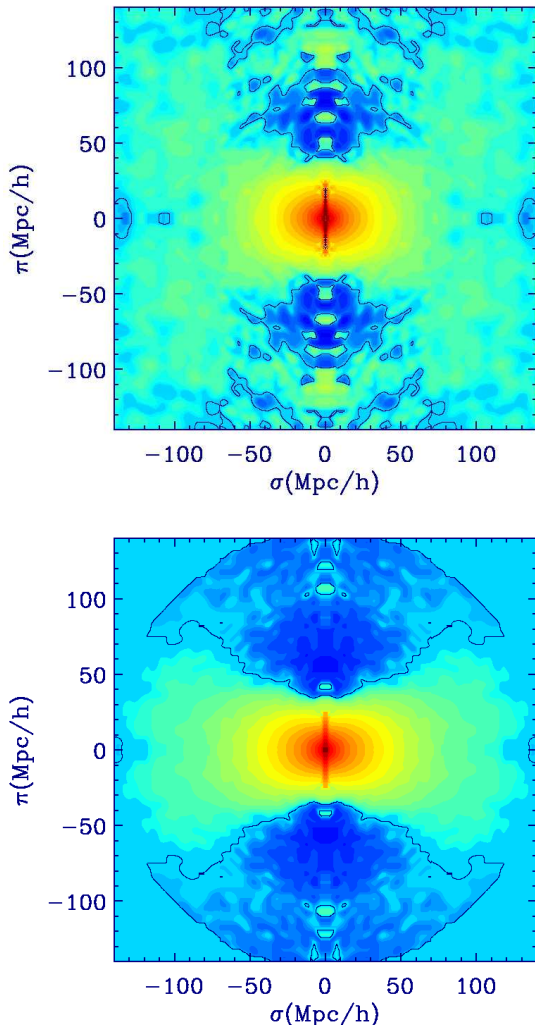


FIG. 16: 2-point anisotropic redshift correlation function $\xi(\sigma, \pi)$ for LRG galaxies in DR6 catalog (top panel) and mock MICE simulations (bottom panel, with a linear bias $b=2$, in order to be similar in amplitude to real LRG). Contours are -0.5 to -0.004 with logarithmic bin of 0.4 , 0 . (over-plotted as a line), 0.003 to 40 . with $\log \text{bin}=0.4$. We see how the real LRG have a less flattened shape around the center, since β is smaller because of bias

SDSS catalog. The random catalog has the same redshift (radial) distribution as the data, but smoothed with a bin $dz = 0.01$ to avoid the elimination of intrinsic correlations in the data. Randoms also have the same mask. We count the pairs in bins of separation along the line-of-sight (LOS), π , and across the sky, σ . The LOS distance π is just the difference between the radial comoving distances in the pair. The perpendicular distance between the two particles corresponds approximately to the mean redshift. It is exactly defined here as $\sigma = \sqrt{s^2 - \pi^2}$, where s is the distance between the particles. We use the wide-angle approximation, as if we had the catalog at an infinite distance, which is accurate until the angle

that separates the galaxy pair in the sky is larger than 15deg for the quadrupole and below for the $\xi(\sigma, \pi)$, about 10 degrees (see Szapudi [38] and Matsubara [33]). This condition corresponds to scales larger than $\sigma = 80\text{Mpc}/h$ for our mean catalog, at an angle= 10deg .

In Fig.16 we can see our $\xi(\sigma, \pi)$ estimation for LRG DR6 catalog and for MICE simulations (with a linear bias= 2 to see similarities visually). Here we can clearly see the FOG at small σ as we have increased the pixel resolution when we approach the central part of the image (pixel size varies from $0.2\text{Mpc}/h$ in the center to $10\text{Mpc}/h$ at large scales). As expected, simulations have less noise because we have done the mean over 216 mocks. Moreover, the distortion parameter β is higher in the simulations than in data because of the high bias of LRG, as can be seen in the shape of the 2-point correlation function, which gets more flattened as β increases. We see clearly the baryonic peak, as a ring in the correlation function $\xi(\sigma, \pi)$. This feature will be studied in detail in Paper IV of this series. In next sections we will analyze all the information hidden in this figure, using the analytical form of the error (see §III B).

A. Quadrupole and β estimation

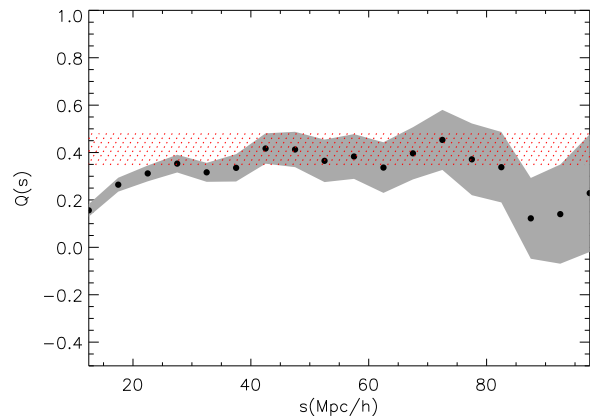


FIG. 17: $Q(s)$ (points with errors) and best fit asymptotic value of β at large scales (Eq.(18)) translated to the quadrupole (red dotted)

As explained in §III E, we use the normalized quadrupole $Q(s)$ to obtain $\beta - \sigma_v$. But first, we can measure β using the asymptotic large scale value in the quadrupole where there is no dependence in σ_v . We find $\beta = 0.34 \pm 0.06$ in the range $40-80\text{Mpc}/h$; $\beta = 0.32 \pm 0.08$ for $50-80\text{Mpc}/h$ and $\beta = 0.34 \pm 0.05$ for $40-100\text{Mpc}/h$. In Fig. 17 we see the quadrupole with jackknife errors at large scales and the error obtained in β , translated to the quadrupole as a band of red dots.

As mentioned above, the quadrupole only depends strongly on β and σ_v . It does not depend on linear bias

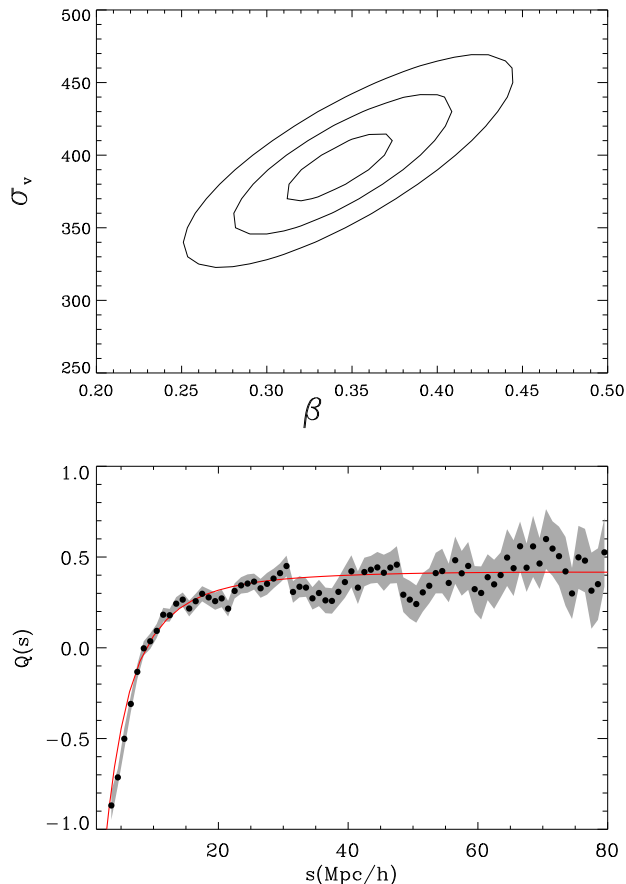


FIG. 18: Top panel: Contour for σ_v and β obtained from the quadrupole $Q(s)$ for the slice $z=0.15-0.47$ at distances between 5-60Mpc/h. Bottom panel: Measured $Q(s)$ (dots with error) and overplotted the best fit (solid red)

because it cancels out in the ratio, and it does not depend much on the shape of the 2-point correlation function (Ω_m and other parameters) or in the non-linear bias for small scales. We have tried to fit β and σ_v using all the scales in the quadrupole, fixing Ω_m to 0.25 (which in our model means fixing the shape of the real-space correlation function) and we use a power law form for the non-linear bias. When we change the shape of the $\xi(r)$ in the model (that is Ω_m for large scales and non-linear bias for small scales), we obtain the same contours for $\beta-\sigma_v$, so we arrive to the conclusion that the normalized quadrupole is a good estimator to find β separately from the other parameters, which are degenerate with them in the $\xi(\pi, \sigma)$ plane.

We can obtain better errors in β by doing a joint fit with σ_v and using smaller scales, as we did in simulations. We will fit the quadrupole above 5Mpc, because this seems a reliable scale according to simulations and results do not change much when using a cut on larger scales. Below this minimum scale, σ_v starts increasing, and even when this has only a small effect in the quadrupole at larger scales, it can bias the value of

Sample	β	σ_v (km/s)
$z=0.15-0.47$	0.310-0.375	365-415
$z=0.15-0.34$	0.280-0.365	320-410
$z=0.34-0.47$	0.305-0.405	345-420
$z=0.15-0.30$	0.280-0.395	305-435
$z=0.30-0.40$	0.285-0.365	335-390
$z=0.40-0.47$	0.270-0.415	305-420

TABLE I: Marginalized values for β and σ_v to 1- σ errors for each sample in redshift obtained from the study of the quadrupole $Q(s)$. We can see that β is nearly constant along the different redshift slices

β when doing a fit to all scales.

In Fig.18 we show the fit as $\Delta\chi^2$ contours in the $\beta-\sigma_v$ plane (top panel) and the best fit to $Q(s)$ for the mean slice (bottom panel). We have fit $\beta-\sigma_v$ for different slices in redshift. First, we divide the catalog in 3 redshift slices: $z=0.15-0.3$, $z=0.3-0.4$, $z=0.4-0.47$. And then, we divide it in 2 redshift slices: $z=0.15-0.34$, $z=0.34-0.47$. The fitted values σ_v and β are similar in all the redshift slices (see table I). This is a bit surprising because we expect $f = \Omega_m(z)^{0.55}$ to increase slightly with z , for this redshift range. The similarity in the value of the distortion parameter β means that the bias must also increase as a function of redshift, roughly in the same way as $f = \Omega_m(z)^{0.55}$ so that the effect cancels out (see Eq.(3)). This is not totally surprising, because we expect bias b to scale with redshift as $1/D(z)$, the inverse of the growth factor, $D(z)$, which is proportional to f .

B. Fitting $\xi(r)$

We have calculated the real-space correlation function integrating through the LOS direction (Eq.(21)). This method is complementary to the estimation from angular correlation [39]. In Fig.19 we compare $\xi(r)$ (in blue) with the monopole $\xi(s)$ (orange). The difference at large scales is a constant value, at least for $r \leq 30Mpc/h$ where we can trust the recovered $\xi(r)$. Note that, although we expect the recovered $\xi(r)$ to be systematically biased at large scales (eg see Fig1), we can still see the baryonic peak at $\xi(r)$, in real space! So this is a strong feature in the LRG data.

The large differences at small scales are due to random velocities, which we will study in more detail in Paper II of this series.

In Fig.20 we show the ratio $\xi(s)/\xi(r)$ and we have overplotted the constant value in the Kaiser approximation (Eq.(23)), using to value of β obtained with $Q(s)$, ie $\beta = 0.34$. This gives a good fit but note how it would be quite difficult to estimate β from this ratio given how noisy the data becomes when we reach an asymptotic constant value in $\xi(s)/\xi(r)$.

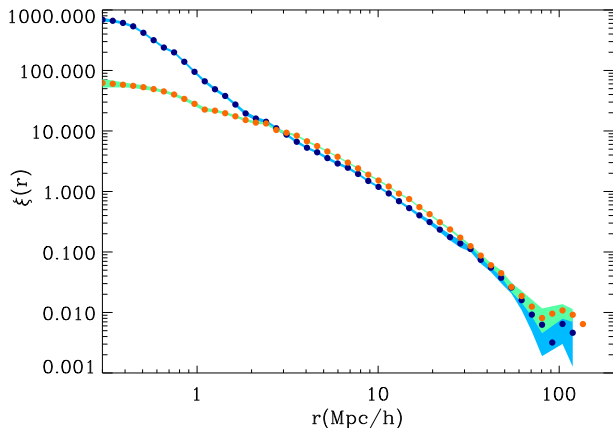


FIG. 19: Real-space correlation function $\xi(r)$ (blue dots) and monopole in redshift space $\xi(s)$ (orange dots). We see clearly how the redshift-space correlation function is the real-space correlation function biased by a constant factor that represents gravitational infall (dependent on β in Kaiser approximation) at scales above 4Mpc/h. However, for small scales, the redshift-space $\xi(s)$ is strongly suppressed compared to $\xi(r)$ due to random peculiar velocities.

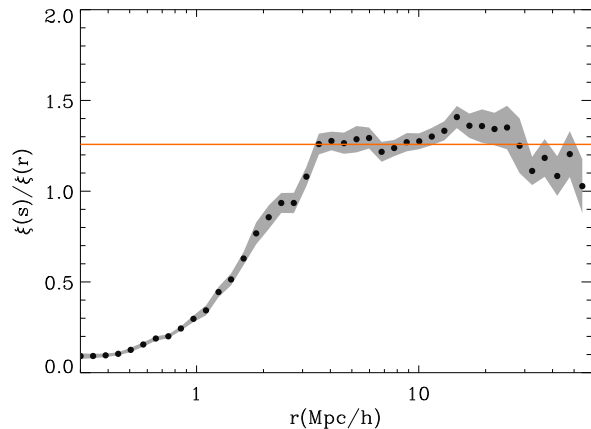


FIG. 20: We plot here the ratio $\xi(s)/\xi(r)$, and its prediction for large scales (Eq.(23)) using $\beta = 0.34$ obtained from the quadrupole $Q(s)$ (solid red line)

C. Fitting large scales in $\xi(\pi, \sigma)$

As explained in §III E, we obtain $\Omega_m - Amp$ from the anisotropic redshift-space correlation function $\xi(\sigma, \pi)$ using the full covariance matrix from the MICE group mocks. Here Amp refers to the factor $b(z)\sigma_8$. The growth factor $D(z)$, which is a function of Ω_m , has been included in the model of $\xi(\pi, \sigma)$. We do not find any difference when fitting $\xi(\sigma, \pi)$ with models with non-linear bias (as used in Paper-II) or linear bias. This is because we restrict our analysis to scales from 20Mpc/h to 60Mpc/h and for angles above 30-40 deg away from the line-of-sight in the $\sigma - \pi$ plane.

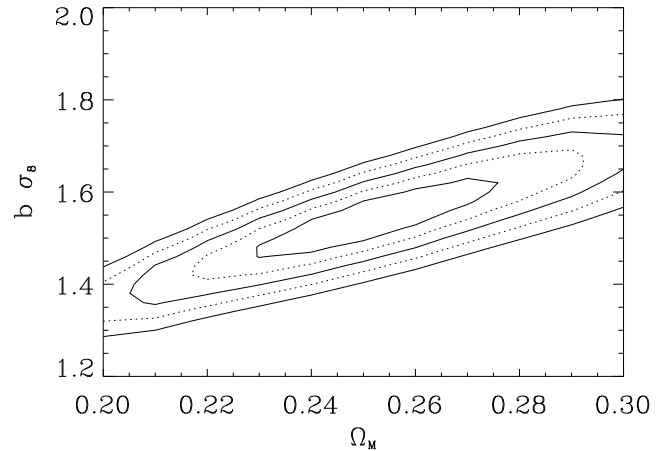


FIG. 21: $z=0.15-0.34$. Contours for Ω_m and $Amp = b\sigma_8$, from a fit to $\xi(\pi, \sigma)$ on large scales. We have marginalized for $\beta - \sigma_v$, using priors from the quadrupole $Q(s)$. Solid lines are 1 - σ , 2 - σ and 3 - σ (1 dof), and dotted lines 1 - σ and 2 - σ (2 dof)

Sample	$Amp = b\sigma_8$	Ω_m	b	$f(\Omega_m)$
$z=0.15-0.47$	1.47-1.65	0.225-0.265	1.73-1.94	0.54-0.73
$z=0.15-0.34$	1.45-1.62	0.230-0.275	1.71-1.91	0.48-0.70
$z=0.34-0.47$	1.55-1.82	0.215-0.285	1.82-2.14	0.56-0.87
$z=0.15-0.30$	1.45-1.80	0.240-0.320	1.71-2.11	0.48-0.83
$z=0.30-0.40$	1.42-1.60	0.210-0.260	1.67-1.88	0.48-0.69
$z=0.40-0.47$	1.60-2.00	0.195-0.305	1.88-2.35	0.51-0.98

TABLE II: Marginalized 1-sigma intervals for $Amp = b\sigma_8$, Ω_m , b and $f(\Omega_m)$ for each redshift sample. Here for b we used the best fit values of $\sigma_8 = 0.85$ for the whole sample.

In Fig.21 we show constraints on $\Omega_m - Amp$ for the slice $z=0.15-0.34$. We have used the $\beta - \sigma_v$ obtained with the quadrupole $Q(s)$ fit to marginalize the space of parameters $\Omega_m - Amp - \beta - \sigma_v$ in the $\xi(\pi, \sigma)$ fit, although this only makes a slight difference. The values of β and σ_v are strongly degenerated in the range where we fit large scales, but σ_v is not strongly degenerated with the other parameters, since we are located away from the fingers of God, where we have the strongest effect of σ_v . When we marginalize, we assume that the likelihood scales as $exp(-\chi^2/2)$.

We have done the same analysis for different redshift slices. We have summarized the results in table II where we have annotated the marginalized 1- σ errors for the amplitude $Amp=b\sigma_8 b$ and for Ω_m .

If we try to fit to even larger scales, we always obtain a slightly biased low Ω_m compared to the one we obtain in the scales before the acoustic peak, probably because the wide-angle approximation but possibly also because non-linear effects on the BAO peak and large sampling errors. We have also seen this effect in the simulations, where we have checked that the best region to obtain

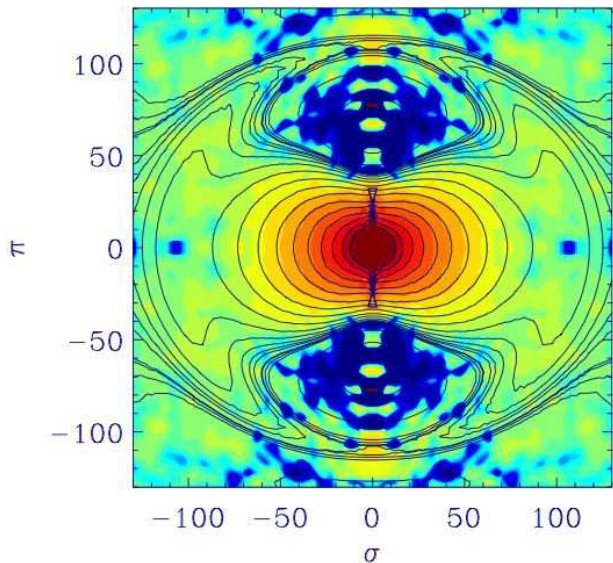


FIG. 22: Best Hamilton model fit (solid lines) to the 2-point anisotropic redshift correlation function $\xi(\sigma, \pi)$ for LRG galaxies (colors). Colors are as in Fig.13). The agreement with the model is excellent at all levels.

parameters is at intermediate to large scales, where we do our fit.

Note how the best fit values of $Amp = b\sigma_8$ seem to change from sample to sample. This could be due to bias, which is both a function of z and luminosity. The values of Ω_m agree within $1 - \sigma$ for 2 degrees of freedom (dotted lines).

In Fig.22 we have plotted the $\xi(\sigma, \pi)$ with the best model overplotted in solid lines. We can see how this simple Kaiser model can explain most features in the observations. There is a very good agreement on the region of negative correlation (in blue) which is a very good tracer of Ω_m and Ω_b (see Paper IV). All these features are very significant given the errors and their coherence over large regions. We can clearly see the FOG at small σ as we have increased the pixel resolution when we approach the central part of the image (pixel size varies from 0.2 Mpc/h in the center to 5 Mpc/h at large scales). The baryonic peak can also be seen in both the data and in the models. The significance of this is studied in detail in Paper IV, while the smaller scales and the prominent fingers of God are presented in Paper II [17].

D. The value of σ_8

We first try to obtain a fit to the parameter σ_8 , which we can separate from the bias $b(z)$ thanks to redshift distortions, following Eq.3 and Eq.4. We use our previous estimation of $\Omega_m - Amp$ from large scales (ie Table II) and the value of β from Q(s) (ie in Table I), using $\gamma = 0.55$, for standard gravity. As $Amp = b(z)\sigma_8$, we obtain

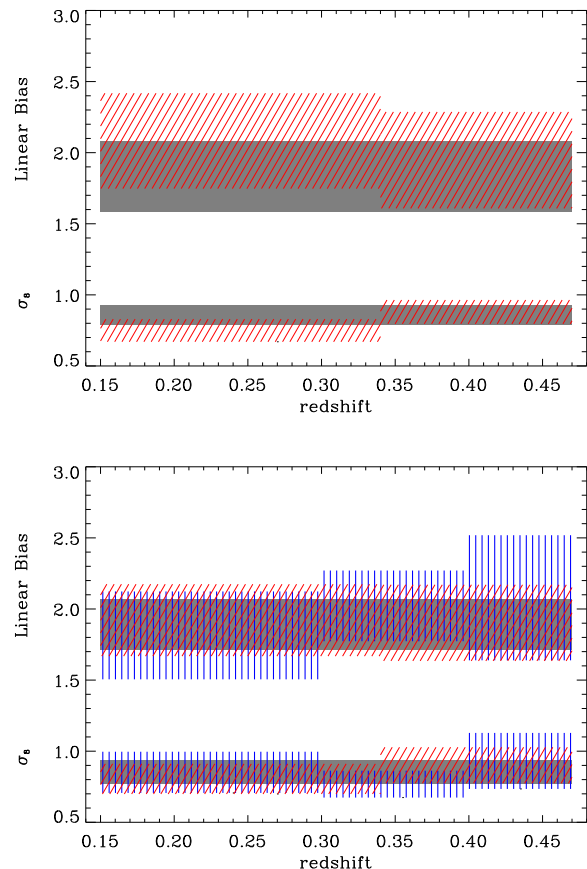


FIG. 23: Estimation of linear bias, $b(z)$, and σ_8 for each slice in redshift. Gray: All the catalog, Red: $z=0.15-0.34$, $z=0.34-0.47$, Blue: $z=0.15-0.3$, $z=0.3-0.4$, $z=0.4-0.47$. In the top panel we marginalized the values over the values of β , Ω_m and $Amp = b(z)\sigma_8$ in each of the 3 samples shown. In the bottom panel we used a fixed best fit value of $\Omega_m = 0.25$ and show results for all subsamples.

σ_8 from:

$$\sigma_8 = \frac{\beta Amp}{\Omega_m(z)^{0.55}} \quad (31)$$

where $\Omega_m(z)$ is given in Eq.5. We also assume a flat universe (WMAP results motivated) with a constant dark energy equation of state characterized by $w = -1$ (ie as in the cosmological constant model).

In the top panel of Fig.23 we show σ_8 , marginalized over β , Amp and Ω_m in each sample. We also show results using a fixed value of Ω_m for all samples (bottom panel). There seems to be a lower σ_8 detection for the middle slice of $z=0.3-0.4$, but it is consistent with the others at $2 - \sigma$ level. In the same figures we also show the estimated bias $b(z)$ from the amplitude Amp and the values σ_8 . For a fixed Ω_m , the linear bias $b(z)$ seems higher as we move to higher redshifts, and it is consistent

with previous results found also with LRG. Note that the luminosity of the galaxies also increases with redshift and this is probably the main reason for the increase in b (more luminous galaxies trace higher density peaks and therefore are more biased). There is one exception to this tendency in slice $z = 0.30 - 0.40$. The values of b for the best fit $\sigma_8 = 0.85$ are shown in Table II, where we can see how b is lower for $z = 0.30 - 0.40$. This is due to the LRG selection explained in §IV, which includes a population of less luminous galaxies $M_r > -21.5$ at $z \simeq 0.35$ (see Fig.43) resulting in a lower bias.

Once we know the bias we can use the values of β to estimate the linear velocity growth function $f(\Omega_m)$ for each slice, which are also shown in Table II.

E. Modified gravity

We can also use redshift distortions to constrain modified gravity. For standard gravity, the linear theory growth factor, $D(a) = \delta/\delta(0)$, depends purely on the expansion history $H(a)$, $w(a)$, $\Omega_m(a)$. Any discrepancy found between the observed growth factor and predictions based on the expansion history can be used to test the gravity.

The idea of using the growth of structure to test gravity has a long history and dates back to Brans-Dicke (BD) model (see [40] for a historical review). More recently, after cosmic acceleration, the BD and variations have been revisited to explore structure formation outside general relativity (Gaztañaga and Lobo [41], see also [42, 43, 44] and references therein). Zhang et al. [45] propose a test to discriminate gravity at cosmological scales based on lensing. Nesseris and Perivolaropoulos [46] have compiled a data set of various data points at a redshift range that can be used to constrain the linear perturbation growth rate f through redshift distortions or indirectly through the rms mass fluctuation $\sigma_8(z)$ inferred from $Ly - \alpha$. Wang [47] do a prediction of the characteristics that a survey must accomplish to be able to rule out the DGP gravity model (an extra-dimensional modification of gravity), where the idea is to calculate $H(z)$ from the baryon acoustic peak and $f(z)$ from redshift distortions. Guzzo et al. [4] test the nature of cosmic acceleration using galaxy redshift distortions at $z=0.8$, obtaining f , but errors are still too high to distinguish between different theories. Acquaviva et al. [44] has recently done a new compilation of results. See Bertschinger and Zukin [48] for a theoretical approach to modified gravity.

If we fix a value for σ_8 , which can also be known from other observations, such as WMAP, we can assume that the changes in the $\xi(\pi, \sigma)$ amplitude with redshift could be explained by changes in the growth factor $D(z)$ due to a different law of gravity at cosmological scales (Linder [3]). This can be represented by the growth index γ . Both $f(z)$ and the growth factor $D(z)$ changes with γ . We have plotted in Fig.24 how f and D change with γ for $z=0.34$ (mean redshift in LRG) and $\Omega_m = 0.25$.

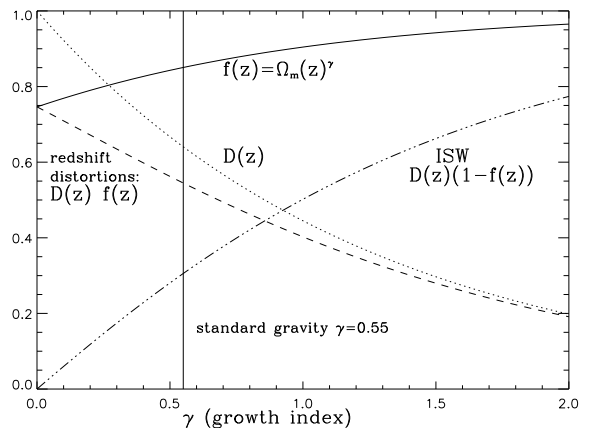


FIG. 24: We see here the change of f and D with γ and the factors involved in redshift distortions and ISW effect. We have fixed $\Omega_m = 0.25$ and $z = 0.34$, as in the main LRG catalog

The measured $\xi(\pi, \sigma)$ amplitude on large scales depends linearly on the product $\sigma_8 b(z)D(z)$. If we now fix σ_8 we can have an estimation of $b(z)D(z)$ as well as our separate estimation of β , from the Quadrupole. We therefore can use this combined data to produce an estimate of $f(z)D(z)$.

We have assumed that the observations can be explained by varying γ , for a fixed dark energy equation of state w . This is a good approximation because w only depends slightly on γ (Linder [49]). We show in Fig.25 our estimation of $1 - \sigma$ errors for the growth index γ once we fix $\sigma_8=0.7, 0.8, 0.9$ and marginalized over β , Amp and Ω_m . As shown in Fig.24, the product $f(\gamma)D(\gamma)$, at a given redshift, decreases with γ . If we change the value σ_8 to higher values, the factor $\beta b(z_{slice}) D(z_{slice})$ obtained from observations will be lower, and this needs to be compensated by reducing $f D$, thus increasing γ . In next section (§VF) we will show how the argument goes in the opposite way when we work with ISW effect. At $2 - \sigma$ and for all the redshift slices, γ is consistent with a standard gravity, except for $\sigma_8 = 0.7$ where we need $3 - \sigma$ for the last slice, favoring a σ_8 clearly higher than 0.7, which is in agreement with recent observations.

Following this argument, we can calculate which is the range of σ_8 that is consistent with standard gravity, $\gamma = 0.55$. We find $0.80 \leq \sigma_8 \leq 0.92$ at $1 - \sigma$. In the modified gravity DGP model, σ_8 needs to be higher since γ is also higher ($\gamma = 0.68$). We could say that DGP model is inconsistent with data if $\sigma_8 < 0.84$. These results are in agreement with the recent study of Yamamoto et al. [5], which appear as we were writing this paper.

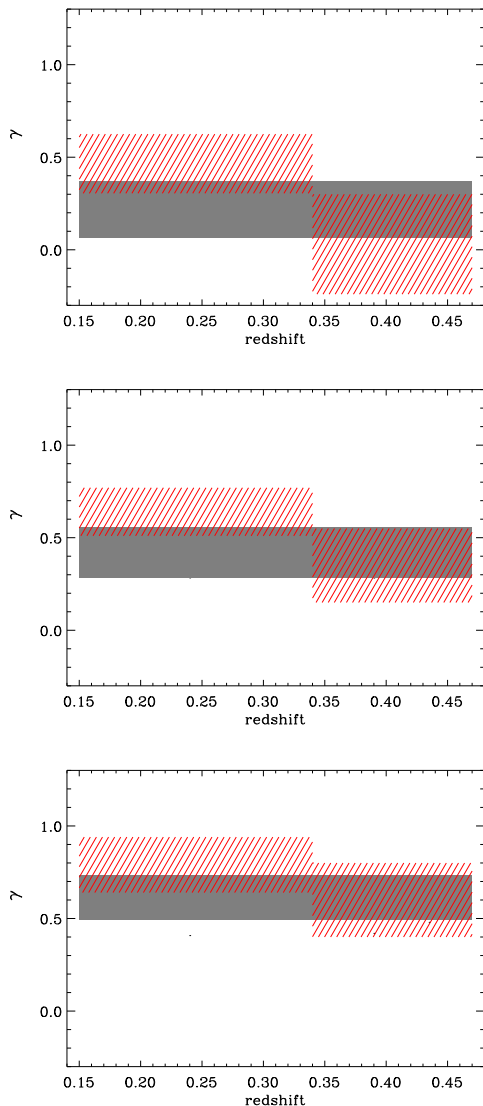


FIG. 25: Growth index γ for different redshift slices as in top panel of Fig.23 when we fix $\sigma_8 = 0.7, 0.8, 0.9$ (from top to bottom). As we increase σ_8 we find that γ also wants to be higher, in favor of modified gravity, such as DGP, where $\gamma = 0.68$ (in standard gravity $\gamma = 0.55$)

F. Angular correlation and cross-correlation with WMAP

We can also learn about the growth of fluctuations using the ISW effect. This method is independent to the one explained before with redshift distortions (see Cabré et al. [50] and references therein for an explanation of the ISW effect in the context of SDSS galaxies). In this section we explore the angular correlation function and also the ISW effect through the cross-correlation between galaxies and fluctuations of temperature in WMAP. Fig.26 shows the results for w_{GG} and w_{TG} at the redshift slice $z=0.15-0.34$. This is the same

data that we have used before, but we now look at angular clustering. The angular auto-correlation function w_{GG} scales as:

$$w_{GG} \propto \sigma_8^2 \phi_G(z)^2 b(z)^2 D(z)^2, \quad (32)$$

while the cross-correlation function between galaxies and CMB temperature fluctuations w_{TG} is proportional to

$$w_{TG} \propto \sigma_8^2 \phi_G(z) b(z) D(z) \frac{d[D(z)/a]}{dz}, \quad (33)$$

where

$$\frac{d[D(z)/a]}{dz} = D(z)(1-f) \quad (34)$$

and $\phi_G(z)$ is the galaxy selection function. Both w_{GG} and w_{TG} are proportional to σ_8^2 because this factor comes from the normalization of the power spectrum, but w_{GG} is proportional to $(\phi_G(z)b(z)D(z))^2$ while w_{TG} is proportional to $(\phi_G(z)b(z)D(z))$ (from the clustering of galaxies) and $\frac{d[D(z)/a]}{dz}$ (from the evolution of gravitational potentials). Thus, this allows for a separate estimation of these quantities [51].

We find that the measured signal of w_{TG} in Fig.26 is higher than expected, a clear tendency that has been seen before (see Giannantonio et al. [52] for a compilation of ISW observations). The high signal w_{TG} could be due to: higher σ_8 , lower Ω_m lower, non-linear effects, bias between matter and galaxies different from the one obtained from galaxies-galaxies, non-linear bias, different form of dark energy as $w > -1$ (see Cabré et al. [28] for some hints in this direction), modified gravity at cosmological scales, or non-linear magnification (linear magnification is not expected to affect ISW at low redshifts, Loverde et al. [53]).

The signal to noise is not very high so we can not obtain tight constraints, but we can explore what could be creating this high signal. We study two reasons here: a change in σ_8 or a change in the growth index γ . We have also studied these two parameters in the section above of redshift distortions and we want to see if results are compatible.

We can break the degeneracy between $b(z)$ and σ_8 in the auto-correlation function w_{GG} , which is proportional to $b^2 \sigma_8^2$, by combining the result with w_{TG} , which goes as $b \sigma_8^2$. We will assume that $b(z)D(z) = b(\bar{z}_{slice})D(\bar{z}_{slice})$ is constant through all the redshift slice, to be consistent with the previous section of redshift distortions.

We fix the shape ($\Omega_m = 0.25$ and flat universe) of w_{GG} and use the amplitude to find the factor $b(\bar{z}_{slice})D(\bar{z}_{slice})\sigma_8$. This should be equal to the amplitude that we found in previous sections, when analyzing 3D redshift distortions, since we are working with the same LRG galaxy samples. We find that this is the

case: both measurements of the amplitude are consistent within the errors. We next fix the dark energy equation of state parameter to $w = -1$ and $\gamma = 0.55$ to standard gravity. We now try to explain the observed amplitude of w_{TG} by just changing σ_8 . We therefore break the degeneracy of σ_8 with bias $b(z)$ in a way that is completely independent from the one used in the previous section, based on 3D redshift distortions. In bottom panel of Fig.26, we have compared w_{TG} to the best model (in red) which corresponds to $\sigma_8 = 1.2$. This value is quite high but errors in w_{TG} are quite large, so that at $1-\sigma$ (or $2-\sigma$ for some of the redshift slices), the values of σ_8 are consistent with our previous estimation.

We next see how we could explain the observed high ISW signal if it is due to a modification of gravity. We fix $\sigma_8 = 0.8$ and vary γ . We assume that $w(z)$ changes only slightly with γ and that almost all the variation with γ in ISW comes from the factor $D(1-f)$. Both D and $(1-f)$ grow with γ , so that $D(1-f)$ also grows with γ (see Fig.24). Thus if we fix σ_8 to a low value we need larger values of γ from the ISW effect, but lower values of γ from redshift space distortions. Thus, this seems to be a promising test because both ways to obtain the growth histories seem to be constrained by data in opposite directions (ie see Fig.24), and we therefore can use these test to break degeneracies in future surveys with better ISW signal-to-noise. For the slice $z=0.15-0.34$ and for a $\sigma_8 = 0.8$, we find that γ needs to be $\gamma = 0.8$, but errors are in this case really big, fully consistent with standard gravity.

From these observations, we conclude a preference for either a higher σ_8 or equivalently, a higher γ than in standard gravity. But this is only a 2-sigma effect. High power could also be due to cosmic variance. Primordially, we want to remark that ISW can provide independent and complementary information to the growth parameter γ . This issue will be resolved with future surveys.

G. Different redshift slices

We look at the differences between the redshift slices in the monopole (Fig.27), in the projected correlation function $\Xi(\sigma)$ (Fig.28), in the real-space correlation function $\xi(r)$ (Fig.29) and in the ratio $\xi(s)/\xi(r)$ (Fig.30).

As we have seen in section §V A, β is similar for all the redshift slices. We can also see this in Fig.30, which shows that the ratio $\xi(s)/\xi(r)$ is quite similar at large scales, indicating similar values of β (Eq.(23)) in all samples. In some of the cases, there seems to be a turning down of the $\xi(s)/\xi(r)$ ratio at scales larger than 30 Mpc/h. This is due to the bias in the recovered $\xi(r)$ which does not work well for scales larger than 30Mpc/h (ie see Fig.1).

The monopole is approximately a measure of the shape of real-space correlation function for large scales, but scaled up by a function of β similar for all the slices. Looking at the monopole (Fig.27) and also at the pro-

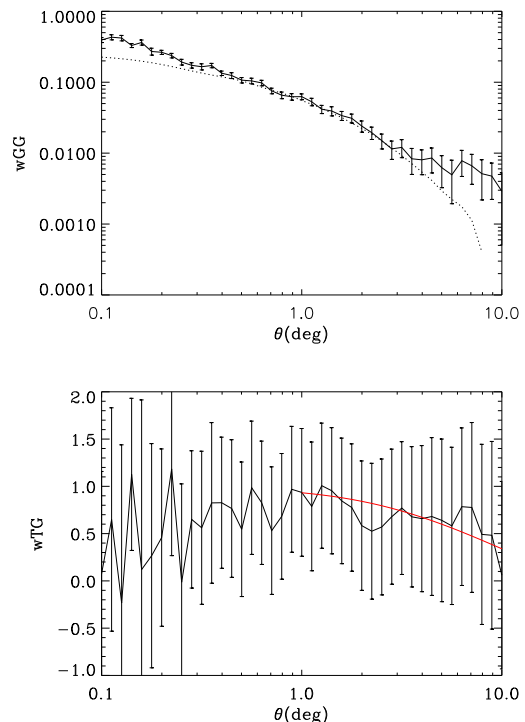


FIG. 26: $z=0.15-0.34$. *Top panel:* w_{GG} of LRGs (solid with errors) and best linear model (dotted line). *Bottom panel:* w_{TG} (solid black with errors) and best model when fitting σ_8 , for $\sigma_8 = 1.2$ and standard gravity, $\gamma = 0.55$ (solid red line).

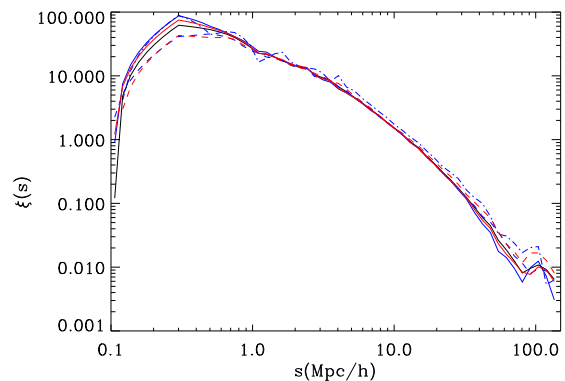


FIG. 27: Comparison between $\xi(s)$ in redshift space for different slices in redshift: All (black), $z=0.15-0.3$ (solid blue), $z=0.3-0.4$ (dashed blue), $z=0.4-0.47$ (dashed-dotted blue); $z=0.15-0.34$ (solid red), $z=0.34-0.47$ (dashed red)

jected correlation function (Fig.28) and at the real-space correlation function (Fig.29) we see that all the slices except from the further one (blue dash-dot) lay in the same line, meaning that $D(z)b(z)$ is almost constant with redshift, what is sometimes called stable clustering.

In Fig.29 we also see that the change of the slope at small scales moves to larger scales as we more to more

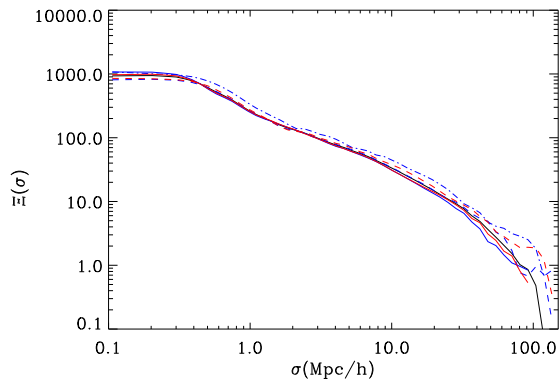


FIG. 28: Comparison between the projected correlation function $\Xi(\sigma)$ for different slices in redshift. All: black, $z=0.15-0.3$ (solid blue), $z=0.3-0.4$ (dashed blue), $z=0.4-0.47$ (dashed-dotted blue); $z=0.15-0.34$ (solid red), $z=0.34-0.47$ (dashed red)

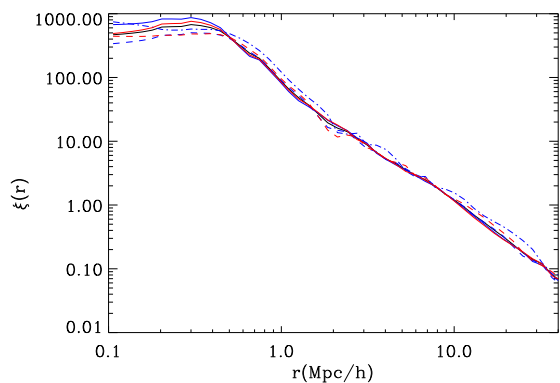


FIG. 29: Comparison between $\xi(r)$ in real space for different slices in redshift. All: black, $z=0.15-0.3$ (solid blue), $z=0.3-0.4$ (dashed blue), $z=0.4-0.47$ (dashed-dotted blue); $z=0.15-0.34$ (solid red), $z=0.34-0.47$ (dashed red)

distant slices. We think that this effect is probably not physical but due to geometry since it corresponds to a fixed angular scale, ie the mask or the fiber collision problem.

Fig.31 shows a zoom over the BAO peak region, as measured in the monopole. This peak is roughly in agreement with predictions and is dominated by modes in the perpendicular direction. The BAO peak is detected in all slices and our best fit model (shown as a continuous line in the Figure) seems a bit lower than the data. This can be fixed by exploring the full parameter space of cosmological models and will be done in Paper IV of this series. This is an important test because it reproduces previous results and indicates that systematic effects can not be too important in our analysis on scales of 100 Mpc/h or smaller. On larger scales, some of the slices show more power than predicted by models. This is compatible with

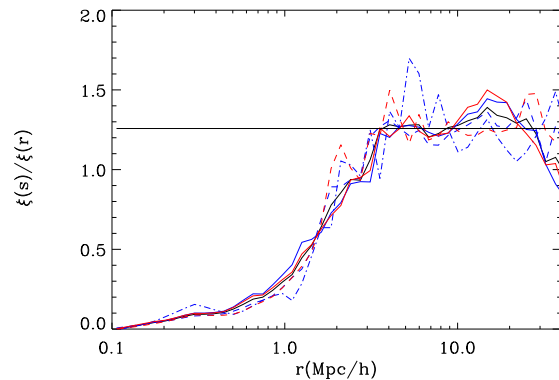


FIG. 30: Comparison between $\xi(s)/\xi(r)$ for different slices in redshift. All: black, $z=0.15-0.3$ (solid blue), $z=0.3-0.4$ (dashed blue), $z=0.4-0.47$ (dashed-dotted blue); $z=0.15-0.34$ (solid red), $z=0.34-0.47$ (dashed red). The constant solid black line shows the Kaiser expression for $\xi(r)/\xi(s)$ at large scales (as a function of β , see Eq.(23)) for $\beta = 0.34$

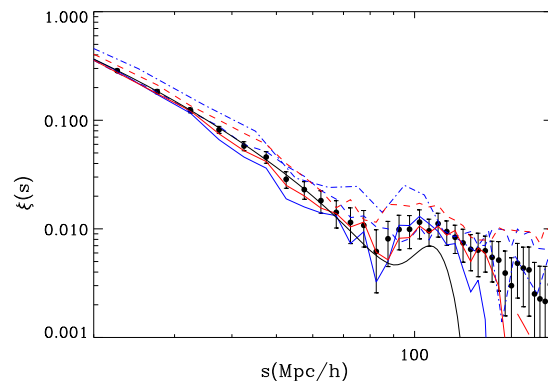


FIG. 31: Comparison between the BAO peak in $\xi(s)$ for different slices in redshift. All: black dots with errors, $z=0.15-0.3$ (solid blue), $z=0.3-0.4$ (dashed blue), $z=0.4-0.47$ (dashed-dotted blue); $z=0.15-0.34$ (solid red), $z=0.34-0.47$ (dashed red). These measurements are compared to the best fit linear model for the principal redshift slice (solid line)

the errors, but we wonder if there could be some hidden systematics here. We will explore this further in the Appendix which is dedicated to the study of systematic effects.

VI. DISCUSSION AND CONCLUSION

In this paper we work with luminous red galaxies (LRGs) from the catalog SDSS DR6 to obtain cosmological parameters from large scales. These are good galaxies to study this range of scales since they trace a big volume of the universe. We use a simple approximation to model the redshift space distortions (see §II), which work incredibly well with LRGs on large scales, as explained

in this paper, but also on small scales, shown in Paper II [17] of this series.

We have used one of the largest N-body simulation run to date (with box size of $L=7680\text{Mpc}/h$ with 2048^3 particles) to create realistic mock LRG galaxy catalogs to analyze the data. We have checked our results to some extent with smaller simulations. This is a crucial step given the complications in the data and the accuracy needed for its interpretation. We have validated all the methods that we used during the paper with credible mock simulations. We also test the validity of the models and the errors: Monte Carlo, jackknife and a theoretical approach for $\xi(\sigma, \pi)$. We find that JK errors does not work properly for large perpendicular distance σ .

There are usually two important sources of statistical errors in clustering analysis: Shot-noise error, due to the finite number of galaxy pairs, and sampling errors, due to the finite amount of volume in the survey. We have shown with our mock simulations that the LRG samples in SDSS DR6 are dominated by the shot-noise term in the 2-point $\xi(\sigma, \pi)$. Usually, this term is assumed to follow the Poisson distribution, with an error given by the inverse of the square root of the number of measurements (ie see Eq.29). This is in fact the case to a good accuracy in our dark matter mocks. But this is not the case for groups of dark matter particles (halos) which are selected in a way that, by construction, the detection of a group creates a large excluding region around the group position. This produces what we have called super-Poisson errors, which are about 40% larger than Poisson errors. Jack-knife errors are shown to be good at detecting this additional shot-noise component and we find that this effect is also present in the real LRG data. This is interpreted here as direct evidence that the dominant fraction of the LRG galaxies populate separate dark matter halos. But this does not exclude a minor fraction of them to populate more than one halo. In fact, in Paper III, [18]), of this series we find evidence for a large quadratic bias which indicates that this is the case [54].

We conclude our discussion on errors by emphasizing the importance of using realistic mocks to assess our results. We have demonstrated here that dark matter mocks are not good enough. Diagonal, sampling errors can in principle be scaled from dark matter to real data because the relative error only depends in the sampling volume. But this is not the case for the shot-noise or for the covariance. The difference is important. Errors and covariances are underestimated with dark matter mocks and results will be wrongly interpreted.

We have calculated the distortion parameter $\beta = [0.310 - 0.375]$ using the normalized quadrupole $Q(s)$, which also provides us of an effective value for the dispersion of random peculiar velocities $\sigma_v = [365 - 415] \text{ km}/s$ (see Table I for more slices in redshift). The great advantage of the normalized quadrupole introduced by Hamil-

ton [19] is that it can measure the squashing produced by bulk galaxy motions with independence of the overall amplitude or shape of the galaxy 2-point correlations. We have also checked if this value for β gives the correct ratio $\xi(s)/\xi(r)$ on large scales. We have shown that with actual data, we can only recover the real-space correlation function $\xi(r)$ for scales smaller than $30\text{Mpc}/h$, and we see that the ratio between the redshift-space monopole $\xi(s)$ and real-space correlation function $\xi(r)$, $\xi(s)/\xi(r)$, can be described by the approximated Kaiser value at large scales, with the same value of β found in the quadrupole.

We obtain a value for Ω_m from the shape of the redshift-space correlation function in the anisotropic plane $\pi - \sigma$ at large scales. The value is $\Omega_m = [0.225 - 0.265]$ for the mean slice (see Table II for other redshift slices). We also obtain a value for the amplitude $b\sigma_8$ in the linear regime. We can therefore break the degeneracy between σ_8 and b thanks to redshift distortions through the parameter β , which results in $\sigma_8 = [0.79 - 0.91]$ and b around 2.

We next look at the growth history and possible modifications of gravity through the parameter γ which is 0.55 for standard gravity and 0.68 for the modified gravity DGP model. We find consistence with standard gravity for $0.8 \leq \sigma_8 \leq 0.92$ at $1-\sigma$. DGP model is inconsistent with our results if $\sigma_8 < 0.84$.

We have also cross-correlated LRGs with WMAP in order to investigate the ISW effect, obtaining a high signal, as in other studies, compared to current ΛCDM model. The degeneracy $b - \sigma_8$ and the growth history can also be studied using the ISW effect which is independent from the study of redshift distortions. The cross-correlation indicates a preference for higher σ_8 .

In the Appendix we look for systematic errors, and arrive to the conclusion that our results are robust in the scales we are doing the analysis.

Acknowledgments

We would like to thank Pablo Fosalba, Francisco Castander, Marc Manera and Martin Crocce for their help and support at different stages of this project. We acknowledge the use of simulations from the MICE consortium (www.ice.cat/mice) developed at the MareNostrum supercomputer (www.bsc.es) and with support from PIC (www.pic.es), the Spanish Ministerio de Ciencia y Tecnologia (MEC), project AYA2006-06341 with EC-FEDER funding, Consolider-Ingenio CSD2007-00060 and research project 2005SGR00728 from Generalitat de Catalunya. AC acknowledge support from the DURSI department of the Generalitat de Catalunya and the European Social Fund.

-
- [1] N. Kaiser, MNRAS **227**, 1 (1987).
- [2] J. K. Adelman-McCarthy, M. A. Agüeros, S. S. Allam, C. Allende Prieto, K. S. J. Anderson, S. F. Anderson, J. Annis, N. A. Bahcall, C. A. L. Bailer-Jones, I. K. Baldry, et al., ApJS **175**, 297 (2008), arXiv:0707.3413.
- [3] E. V. Linder, PRD **72**, 043529 (2005), arXiv:astro-ph/0507263.
- [4] L. Guzzo, M. Pierleoni, B. Meneux, E. Branchini, O. Le Fèvre, C. Marinoni, B. Garilli, J. Blaizot, G. De Lucia, A. Pollo, et al., Nature **451**, 541 (2008), arXiv:0802.1944.
- [5] K. Yamamoto, T. Sato, and G. Huetsi, ArXiv e-prints **805** (2008), 0805.4789.
- [6] T. Giannantonio, R. G. Crittenden, R. C. Nichol, R. Scranton, G. T. Richards, A. D. Myers, R. J. Brunner, A. G. Gray, A. J. Connolly, and D. P. Schneider, PRD **74**, 063520 (2006), arXiv:astro-ph/0607572.
- [7] M. Tegmark, D. J. Eisenstein, M. A. Strauss, D. H. Weinberg, M. R. Blanton, J. A. Frieman, M. Fukugita, J. E. Gunn, A. J. S. Hamilton, G. R. Knapp, et al., PRD **74**, 123507 (2006), arXiv:astro-ph/0608632.
- [8] I. Zehavi, D. J. Eisenstein, R. C. Nichol, M. R. Blanton, D. W. Hogg, J. Brinkmann, J. Loveday, A. Meiksin, D. P. Schneider, and M. Tegmark, ApJ **621**, 22 (2005), arXiv:astro-ph/0411557.
- [9] T. Okumura, T. Matsubara, D. J. Eisenstein, I. Kayo, C. Hikage, A. S. Szalay, and D. P. Schneider, ApJ **676**, 889 (2008), arXiv:0711.3640.
- [10] T. Matsubara, ApJ **615**, 573 (2004), arXiv:astro-ph/0408349.
- [11] D. J. Eisenstein, I. Zehavi, D. W. Hogg, R. Scoccimarro, M. R. Blanton, R. C. Nichol, R. Scranton, H.-J. Seo, M. Tegmark, Z. Zheng, et al., ApJ **633**, 560 (2005), arXiv:astro-ph/0501171.
- [12] G. Hütsi, A&A **449**, 891 (2006), arXiv:astro-ph/0512201.
- [13] G. Hütsi, A&A **459**, 375 (2006), arXiv:astro-ph/0604129.
- [14] W. J. Percival, S. Cole, D. J. Eisenstein, R. C. Nichol, J. A. Peacock, A. C. Pope, and A. S. Szalay, MNRAS **381**, 1053 (2007), arXiv:0705.3323.
- [15] N. Padmanabhan, D. J. Schlegel, U. Seljak, A. Makarov, N. A. Bahcall, M. R. Blanton, J. Brinkmann, D. J. Eisenstein, D. P. Finkbeiner, J. E. Gunn, et al., MNRAS **378**, 852 (2007), arXiv:astro-ph/0605302.
- [16] C. Blake, A. Collister, S. Bridle, and O. Lahav, MNRAS **374**, 1527 (2007), arXiv:astro-ph/0605303.
- [17] A. Cabré and E. Gaztañaga, ArXiv e-prints **2461** (2008), 0807.2461.
- [18] E. Gaztañaga, A. Cabré, F. Castander, M. Crocce, and P. Fosalba, ArXiv e-prints **2448** (2008), 0807.2448.
- [19] A. J. S. Hamilton, ApJ **385**, L5 (1992).
- [20] P. J. E. Peebles, *The large-scale structure of the universe* (Research supported by the National Science Foundation. Princeton, N.J., Princeton University Press, 1980. 435 p., 1980).
- [21] A. Ratcliffe, T. Shanks, Q. A. Parker, A. Broadbent, F. G. Watson, A. P. Oates, C. A. Collins, and R. Fong, VizieR Online Data Catalog **730**, 417 (1998).
- [22] S. D. Landy, ApJ **567**, L1 (2002), arXiv:astro-ph/0202130.
- [23] R. Scoccimarro, PRD **70**, 083007 (2004), arXiv:astro-ph/0407214.
- [24] J. L. Tinker, D. H. Weinberg, and Z. Zheng, MNRAS **368**, 85 (2006), arXiv:astro-ph/0501029.
- [25] J. L. Tinker, MNRAS **374**, 477 (2007), arXiv:astro-ph/0604217.
- [26] M. Davis and P. J. E. Peebles, ApJ **267**, 465 (1983).
- [27] W. Saunders, M. Rowan-Robinson, and A. Lawrence, MNRAS **258**, 134 (1992).
- [28] A. Cabré, E. Gaztañaga, M. Manera, P. Fosalba, and F. Castander, MNRAS **372**, L23 (2006), arXiv:astro-ph/0603690.
- [29] A. E. Evrard, J. Bialek, M. Busha, M. White, S. Habib, K. Heitmann, M. Warren, E. Rasia, G. Tormen, L. Moscardini, et al., ApJ **672**, 122 (2008), arXiv:astro-ph/0702241.
- [30] S. D. Landy and A. S. Szalay, ApJ **412**, 64 (1993).
- [31] R. E. Smith, R. Scoccimarro, and R. K. Sheth, PRD **75**, 063512 (2007), arXiv:astro-ph/0609547.
- [32] E. Hawkins, S. Maddox, S. Cole, O. Lahav, D. S. Madgwick, P. Norberg, J. A. Peacock, I. K. Baldry, C. M. Baugh, J. Bland-Hawthorn, et al., MNRAS **346**, 78 (2003), arXiv:astro-ph/0212375.
- [33] T. Matsubara, ApJ **535**, 1 (2000), arXiv:astro-ph/9908056.
- [34] D. J. Eisenstein, J. Annis, J. E. Gunn, A. S. Szalay, A. J. Connolly, R. C. Nichol, N. A. Bahcall, M. Bernardi, S. Burles, F. J. Castander, et al., AJ **122**, 2267 (2001), arXiv:astro-ph/0108153.
- [35] D. J. Schlegel, D. P. Finkbeiner, and M. Davis, ApJ **500**, 525 (1998), arXiv:astro-ph/9710327.
- [36] D. J. Eisenstein and W. Hu, ApJ **496**, 605 (1998), arXiv:astro-ph/9709112.
- [37] R. E. Smith, J. A. Peacock, A. Jenkins, S. D. M. White, C. S. Frenk, F. R. Pearce, P. A. Thomas, G. Efstathiou, and H. M. P. Couchman, MNRAS **341**, 1311 (2003), arXiv:astro-ph/0207664.
- [38] I. Szapudi, ApJ **614**, 51 (2004), arXiv:astro-ph/0404477.
- [39] C. M. Baugh, MNRAS **280**, 267 (1996), arXiv:astro-ph/9512011.
- [40] C. H. Brans (2005), gr-qc/0506063.
- [41] E. Gaztañaga and J. A. Lobo, ApJ **548**, 47 (2001), arXiv:astro-ph/0003129.
- [42] A. Lue, R. Scoccimarro, and G. Starkman, PRD **69**, 044005 (2004), arXiv:astro-ph/0307034.
- [43] A. Lue, R. Scoccimarro, and G. D. Starkman, PRD **69**, 124015 (2004), arXiv:astro-ph/0401515.
- [44] V. Acquaviva, A. Hajian, D. N. Spergel, and S. Das, ArXiv e-prints **803** (2008), 0803.2236.
- [45] P. Zhang, M. Liguori, R. Bean, and S. Dodelson, Physical Review Letters **99**, 141302 (2007), arXiv:0704.1932.
- [46] S. Nesseris and L. Perivolaropoulos, PRD **77**, 023504 (2008), arXiv:0710.1092.
- [47] Y. Wang, ArXiv e-prints **710** (2007), 0710.3885.
- [48] E. Bertschinger and P. Zukin, ArXiv e-prints **801** (2008), 0801.2431.
- [49] E. V. Linder, ArXiv e-prints **709** (2007), 0709.1113.
- [50] A. Cabré, P. Fosalba, E. Gaztañaga, and M. Manera, MNRAS **381**, 1347 (2007), arXiv:astro-ph/0701393.
- [51] P. Fosalba, E. Gaztañaga, and F. J. Castander, ApJ **597**, L89 (2003), arXiv:astro-ph/0307249.
- [52] T. Giannantonio, R. Scranton, R. G. Crittenden, R. C. Nichol, S. P. Boughn, A. D. Myers, and G. T. Richards, ArXiv e-prints **801** (2008), 0801.4380.

- [53] M. Loverde, L. Hui, and E. Gaztañaga, PRD **75**, 043519 (2007).
- [54] R. Scoccimarro, R. K. Sheth, L. Hui, and B. Jain, ApJ **546**, 20 (2001), arXiv:astro-ph/0006319.
- [55] H. A. Feldman, N. Kaiser, and J. A. Peacock, ApJ **426**, 23 (1994), arXiv:astro-ph/9304022.
- [56] K. M. Górski, E. Hivon, A. J. Banday, B. D. Wandelt, F. K. Hansen, M. Reinecke, and M. Bartelmann, ApJ **622**, 759 (2005), arXiv:astro-ph/0409513.
- [57] C. M. Baugh, D. J. Croton, E. Gaztañaga, P. Norberg, M. Colless, I. K. Baldry, J. Bland-Hawthorn, T. Bridges, R. Cannon, S. Cole, et al., MNRAS **351**, L44 (2004), arXiv:astro-ph/0401405.
- [58] http://cosmo.nyu.edu/blanton/kcorrect/kcorrect_help.html

APPENDIX A: SYSTEMATIC EFFECTS

In this section we look for possible systematic errors that could be imprinted by the radial mask through the line-of-sight, the angular mask, or the selection in LRG galaxies. These systematics effect are typically more important on the largest scales, where the correlation function becomes smaller. In Fig.31 we show that for some slices there is extra power in $\xi(s)$ at scales $s > 130 Mpc/h$, something which is not expected in the models. This is particularly evident for the slice in redshift $z=0.3-0.4$, where the signal-to-noise is small (Amp and bias b are smaller in Table II) and we do not have a significant peak detection. This extra power could be due to sampling variance but could also be caused by some systematic errors in the data or the way we analyze it. The extra power seems to be important at scales larger than the baryonic peak, but we test here if it could also have some effect over the peak location. This extra power has also been detected in other analysis of SDSS LRG around similar scales [15, 16]. We will focus here on systematics related to the way we have analyzed the data, rather than systematics in the data itself. The later has been explored in detail elsewhere (eg Eisenstein et al. [11]).

1. Radial Selection

First, we test the radial selection function that we use for the random catalogs. If we use exactly the same radial density distribution $N(z)$ as selection function of the data, we suppress the radial modes in the π direction. In Fig.32 we can see the differences between different smoothing windows in the data selection function, and in Fig.33 the redshift-space correlation function for these three smoothing bins.

We do not see any significant difference between the three cases indicating that our analysis is robust with respect to the radial selection.

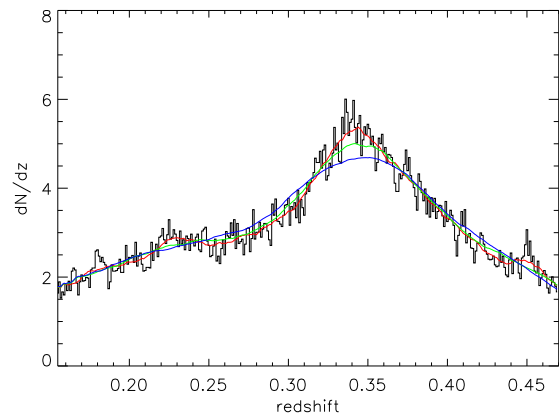


FIG. 32: Selection function for data (black histogram) and smoothed for the random catalogs with a bin in redshift of $z=0.02$ (red), $z=0.05$ (green) and $z=0.08$ (blue)

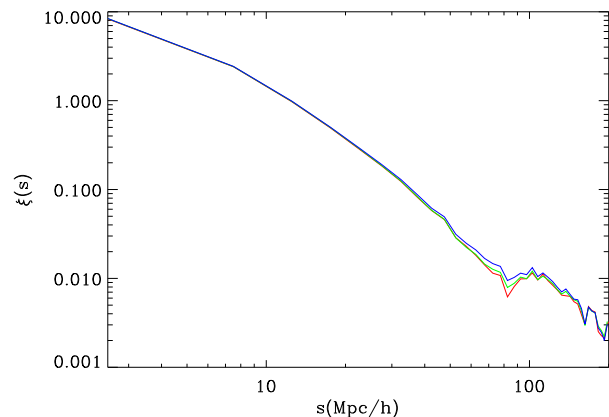


FIG. 33: Redshift-space correlation using different redshift smoothing in the random selection function of 0.02 (red), 0.05 (green) and 0.08 (blue)

2. Weighting

In Fig.35 we compare our results in the monopole (red with shaded region as errors) to that of Eisenstein et al. [11] (in black line with errorbars) for all the sample. Our result is consistent with this previous estimate despite the increase in the DR6 area and the difference in the selection. However, at larger scales than the baryonic peak, we observe some extra-power in our estimation. We wonder if the difference is just due to sampling, selection or to the way we estimate the correlation function (we not include the same weighting as Eisenstein et al. [11]).

We have also calculated the correlation function using a weighting scheme, as the one explained in [11]. We weight the sample using a scale-independent weighting

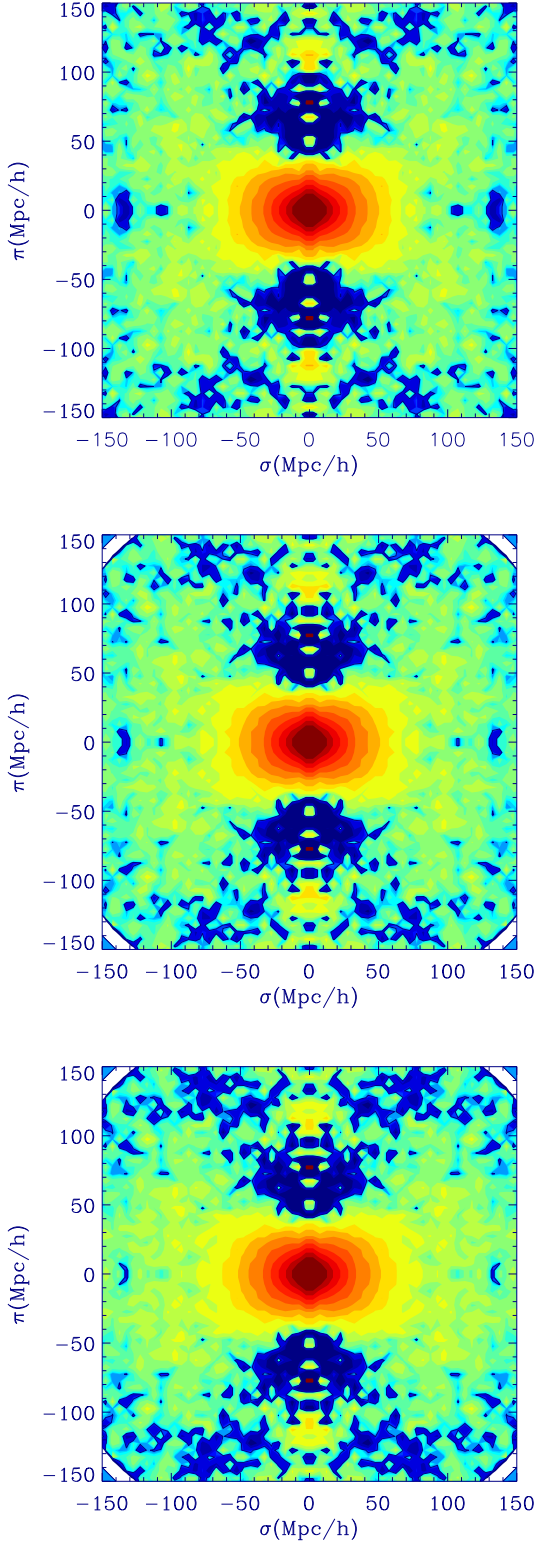


FIG. 34: $\xi(\pi, \sigma)$ correlation using different redshift smoothing in the random selection function of 0.02 (top), 0.05 (middle) and 0.08 (bottom).

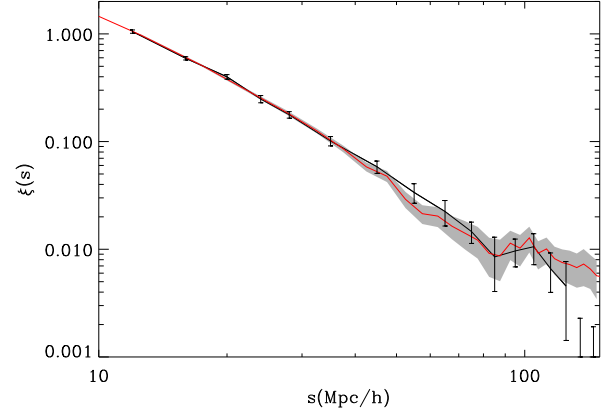


FIG. 35: Estimation of the redshift-space correlation function for LRG. In black line with JK errors correspond to the result by [11]. Over-plotted in red is our result, where the shaded region corresponds to our error estimate.

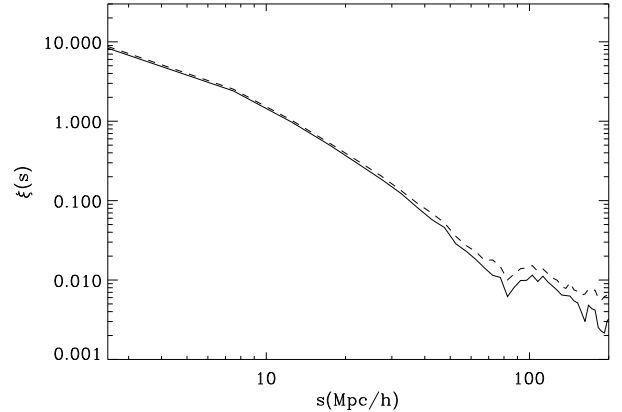


FIG. 36: Our previous estimation of the redshift-space correlation function for LRG (solid) compared to estimation using a weighting as explained in the text (dotted)

that depends on redshift. When computing the correlation function, each galaxy and random point is weighted by $1/(1 + n(z)Pw)$ (Feldman et al. 55) where $n(z)$ is the comoving number density and $Pw = 40,000h^{-3}Mpc^3$. We do not allow Pw to change with scale so as to avoid scale-dependent changes in the effective bias caused by differential changes in the sample redshift. We choose Pw at $k \simeq 0.05hMpc^{-1}$ as in [11]. At $z < 0.36$, nPw is about 4, while $nPw \simeq 1$ at $z = 0.47$.

In Fig.36 we can see the comparison between the correlation function estimated without weighting (solid line) and with weighting (dashed line). Contrary of what we were looking for, the extra power is higher in the weighting scheme, which makes sense, since we are now giving more importance to the higher redshift pairs, which have a larger bias (see below).

In Fig.37 we have plotted the anisotropic correlation

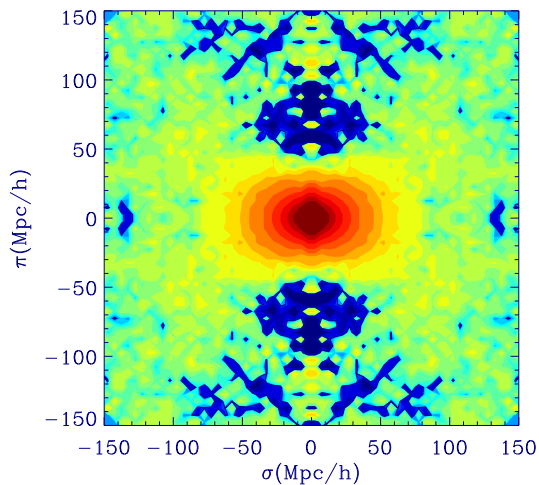
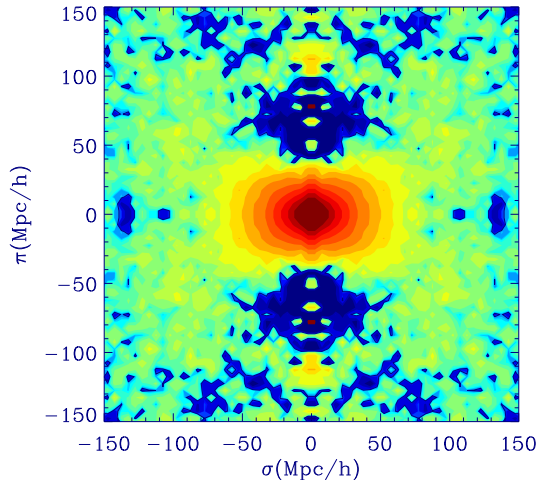


FIG. 37: Our previous estimation of the redshift-space correlation function $\xi(\pi, \sigma)$ for LRG (top panel) compared to estimation using a weighting as explained in the text (bottom panel)

function $\xi(\pi, \sigma)$ for both cases, showing only slight differences. It is apparent that the monopole is more sensitive that $\xi(\pi, \sigma)$ to displace systematic differences. We will therefore concentrate on results for the monopole from now on.

3. Angular Selection

We next look at the angular selection function, the mask. First, we construct a different mask than the original by using a Healpix map [56], with $n_{\text{side}}=64$ (with pixels of area $\simeq 0.8$ sq deg). In Fig.38 we plot the distribution function for the number of galaxies per pixel. The pixel is large enough to distinguish between real empty pixels and artificial ones. We only include pixels that have more than n galaxies, where $n=2,6$ and 10 . As we

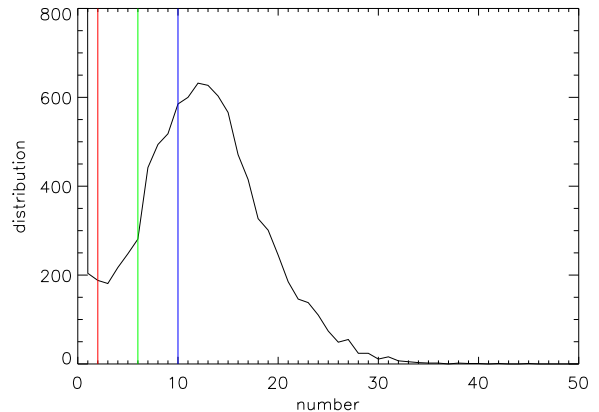


FIG. 38: Distribution function of number of galaxies per pixel ($n_{\text{side}}=64$ using the package Healpix)

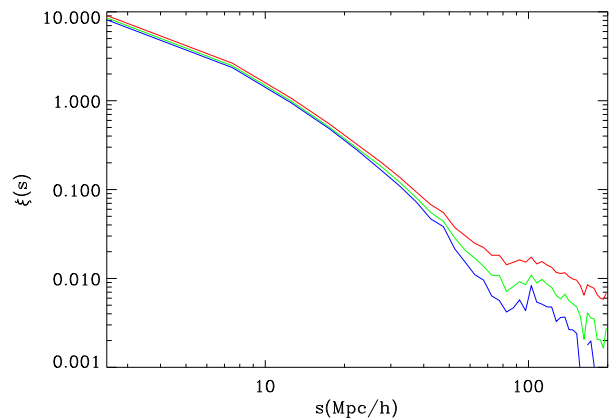


FIG. 39: We now define our catalog by including all the pixels that have more than n galaxies in the Fig.38 ($n>2$ red, $n>6$ green, $n>10$ blue) and plot the redshift-space correlation function

can see in the distribution plot, if we include more than 2 galaxies, we are probably including artificial void zones, which will create extra power and pencil beams at the direction line-of-sight, while when we include only the pixels with more than 10 galaxies, we are probably excluding some real voids. In this second case, the density is higher than the real one, so the density contrast is lower. We can see these effects in Fig.39 for the correlation function in redshift space. We see that the correlation is lower when we increase the minimum number of galaxies (from red to blue), but we can always see the baryonic peak and the three lines have the same shape approximately. Our results are similar to the case $n > 6$, which does not include artificial voids and does not eliminate real voids.

The spectroscopic survey of SDSS is observed using circular plates, which contain about 600 fibers each to take spectra. Targets are selected from the photometric survey, although the spectroscopic survey is not

exactly the same as the photometric one. There are some plates that have not been observed properly due to known problems, which are explained in the web (<http://www.sdss.org>). We have extracted from our previously calculated mask all the galaxies that are not laying inside “good” plates (maskplate1). In Fig.40 we can see the plates (black circles) and the galaxies (red dots). Moreover, we can also eliminate all the galaxies that lay inside a bad plate to ensure that we are taking only the really good ones (maskplate2). This second mask reduces the number of galaxies significantly, and the correlation is then a lot noisier, but we show here the results. In Fig.41 we have plotted the redshift-space averaged correlation function for the new mask based on spectroscopic plates. Results are very similar to our previous result, in black. Moreover, we over-plot the result for the north stripe of SDSS, which contains the most significant part of the survey, in blue. The anisotropic redshift-space correlation function is really similar in all these cases, so that we do not find it useful to plot it.

We have also tried to extract all the plates that have a large number of galaxies, which have big super-clusters, since it is known that big clusters can bias the correlation function for regular galaxies [57]. The result is not significantly modified which could have been expected since LRG in SDSS DR6 cover a much larger volume than 2DFGRS or SDSS for regular galaxies.

4. Volume limited samples

In volume limited surveys, we can estimate the correlation function with a pixelization scheme. The correlation function can then be estimated as:

$$\xi(s) = \sum_{ij} \delta_G(s_i) \delta_G(s_j) / N_{pairs}(s) \quad (A1)$$

where $\delta_G = N_G / \langle N_G \rangle - 1$ and the sum extends to all pairs i, j separated by a distance $s \pm \Delta s$. We have taken a volume limited part of the selected galaxies, with redshift $z=[0.15, 0.38]$ and absolute magnitude $M_r=[-22.5, -21.5]$ and have calculated the correlation using this method. This is the same sample used in Paper IV of this series. We have also calculated a similar selection by using the traditional method with a random catalog. Results are plotted in Fig.42, dotted for the pixel method and solid for the randoms. This is a good test to validate our results, since both methods are quite different. As we can see in the figure, the two estimations are very similar. The slight shift in amplitude at small scales is due to the pixel smoothing, a cube of 10 Mpc/h on the side for this case. This shift can be modeled with a top-hat window function reproducing the exact amplitude difference. There is a very good match using

TABLE III: Slices in the plane $M_r - z$

Sample	M-range	Mean M	mean z	z-range
S22.50	-22.50 -23.00	-22.75	0.43	0.35-0.50
S22.25	-22.25 -22.75	-22.50	0.40	0.33-0.48
S22.00	-22.00 -22.50	-22.25	0.38	0.31-0.46
S21.75h	-21.75 -22.25	-22.00	0.35	0.27-0.42
S21.75	-21.75 -22.25	-22.00	0.20	0.12-0.27
S21.50h	-21.50 -22.00	-21.75	0.32	0.25-0.40
S21.50	-21.50 -22.00	-21.75	0.18	0.10-0.25
S21.25	-21.25 -21.75	-21.50	0.18	0.10-0.25

smaller pixel size. Also note how these estimations, based on a volume limited sample with about half of the LRG galaxies, agree quite well with previous results (ie in Fig.41) which includes all galaxies at a price of a more complicated selection function. Despite all this difference, we see no significant change in $\xi(s)$ at the largest scales.

We have also divided the catalog in different volume limited slices as indicated in table A 4 plotted in Fig.43. The most and less luminous slices (in the bottom right and top left) contain fewer galaxies and have too much noise at the baryonic peak, but we see that the red and pink slices, at intermediate redshifts and magnitudes, contribute to the extra-power that we see at large scales (Fig.44 with the same colors as Fig.43). Note how these subsamples cover a sharp feature at $z=0.35$ in the selection function (eg see Fig.32) which is clearly an artifact of the selection function because of the double selection cut in LRG. This feature is diluted when we consider volume limited samples as we discard the less luminous galaxies $M_r > -21.5$ which contribute most to this peak. As shown above, the correlation $\xi(s)$ for a volume limited sample in the range $M_r=[-22.5, -21.5]$, shown in Fig.42 is in excellent agreement with the one for the whole sample in Fig.35. Thus we conclude that our measurements are quite robust and are not affected by the selection cuts.

We have not plotted larger scales for the other slices because they are quite noisy. However, at intermediate scales, we can see clearly the bias due to different intrinsic luminosity, more biased when more luminous, although bias seems to be independent on scale, in the scales used for our analysis.

5. Wide angle approximation

We have calculated the correlation function limiting the angle between galaxies to see if wide angle effects that are apparent in $\xi(\pi, \sigma)$ disappear. In Fig.45, we see the anisotropic $\xi(\pi, \sigma)$ without limits in the angle (top panel) compare to the one only accepting galaxies with $\theta < 10deg$ (bottom panel). As we increase the restriction, we see how the σ direction recovers power,

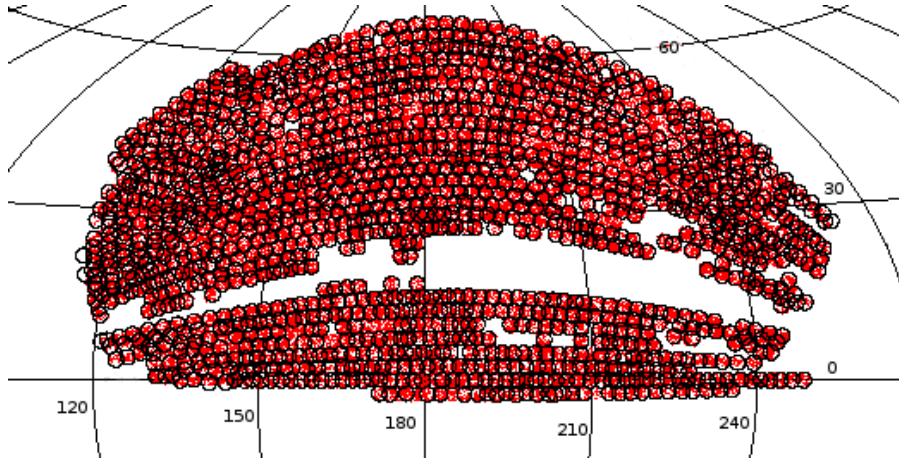


FIG. 40: SDSS DR6 survey with our selection of LRG galaxies as red points and the spectroscopic “good” plates as black circles

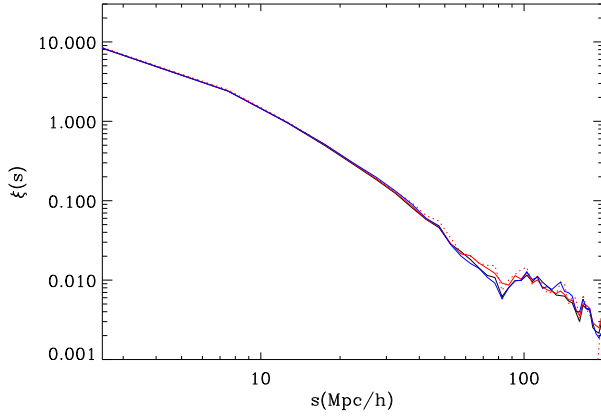


FIG. 41: Redshift-space correlation function for our mask (black), maskplate1 as indicated in the text (red), maskplate2 (dotted red) and north stripe (blue)

which explains the lack of power we saw in the σ direction when angles are too big to apply the distant observer approximation. The angle between galaxies explain part of the distortions due to wide angle effects, specially the ones that are concentrated at small π and large σ , which affect the first slice considered, from $z=0.15-0.3$. The angle γ_z , between the direction LOS (at $\theta/2$) and the vector which goes from galaxy 1 to galaxy 2 (following the notation used in Matsubara 33), is also important and can also imprint some modifications at larger π and large σ .

We conclude that the measurements on the BAO scale are quite robust and the extra power at the largest scales is probably the result of sampling fluctuations and shot noise. For redshifts around $z=0.35$ we find extra noise on large scales, probably due to an artifact in the selection function. In any case, none of the systematics we have

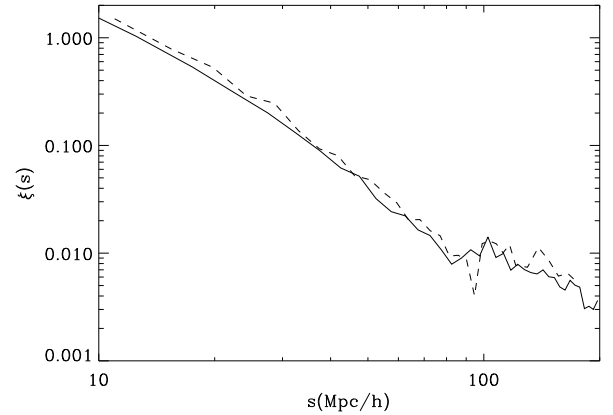


FIG. 42: Redshift-space correlation function for a volume limited slice selection of LRG galaxies with $z=[0.15,0.38]$ and $M_r=[-22.5,-21.5]$. Solid line shows the result when using a random catalog. Dotted line shows a new method based on pixelization which validated the previous results

explored modify the peak detection in a significant way.

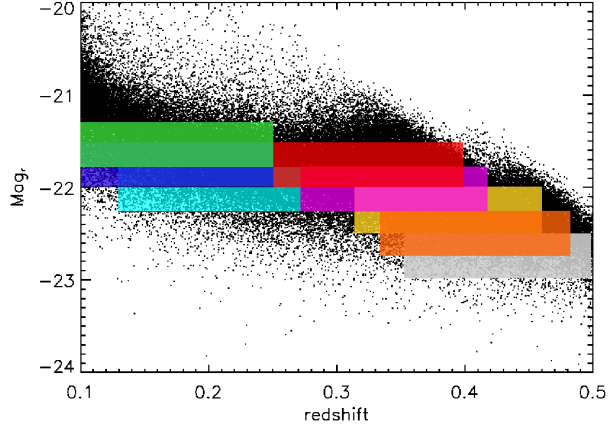


FIG. 43: We have divided the catalog in different approximately volume limited slices as indicated in table A.4. Here we over-plot the slices in the plane $M_r - z$

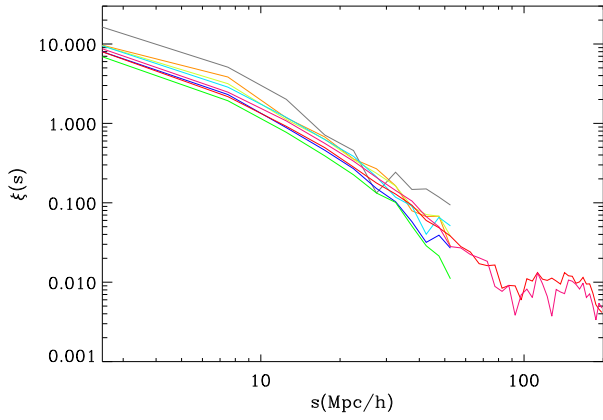


FIG. 44: Redshift-space correlation function for the different slices plotted in Fig.43

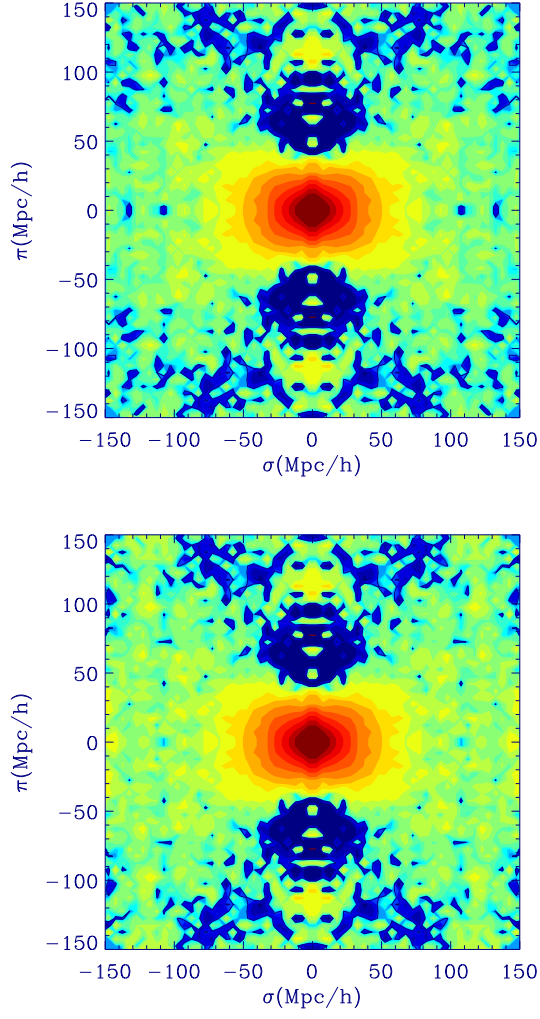


FIG. 45: Redshift-space correlation function $\xi(\pi, \sigma)$ including all the galaxy pairs (top panel) and limiting the angle between galaxies to $\theta < 10 \text{ deg}$ (bottom panel)